



TÉCNICO
LISBOA

**Analysis of in-flight data from ESA's
AlphaSat Environment and Effects Facility
Multi-Functional Spectrometer**

Filipe Máximo Ribeiro Lopes de Carvalho

Thesis to obtain the Master of Science Degree in

Engineering Physics

Supervisors: Prof. Doutora Patrícia Carla Serrano Gonçalves
Doutora Maria Luísa Ferreira da Gama Velho Arruda

Examination Committee

Chairperson: Prof. Doutor Mário João Martins Pimenta
Supervisor: Prof. Doutora Patrícia Carla Serrano Gonçalves
Member of the Committee: Prof. Doutor Ilídio Pereira Lopes

May 2019

Acknowledgments

This thesis sets an important milestone in my life's accomplishments: it represents the conclusion of my masters degree in Engineering Physics and it is in itself my greatest project as a student. Nonetheless, it was only made possible with the support and contribution of others, to whom I'm most grateful.

First and foremost, I thank Prof. Dra. Patrícia Gonçalves, who supervised this work. Her overall support, time and contagious enthusiasm with the subjects of space science were particularly important in keeping me engaged and focused on the objectives of this work. Her supervision was also of great importance in preventing me from going astray and getting lost in my own work and in rescuing me from (what I perceived to be) dead ends that arose throughout time (she always had good ideas!).

I am also very grateful to my cosupervisor Prof. Dra. Luísa Arruda for always being there for me when I needed, by giving me useful materials, tips, advice and feedback, as well as answering my questions.

To all my colleagues that shared their office with me, I thank you for all the support given to me: Ana Luísa, Marco and Jorge for their friendship, tips, discussions and general good mood. Without them I wouldn't have the good moments that I had in the making of this thesis.

I would also take the opportunity to show my appreciation to my family and friends who made me into who I am today. I specially thank my parents for all their support, love and care and my two younger sisters, who support me in their own unique ways.

I thank LIP (Laboratório de Instrumentação e Física Experimental de Partículas) for hosting me and for all the technical support that I (inevitably) required.

Lastly, I thank Susana, who helped me face my inner demons.

Resumo

O MFS é um espectrómetro em GEO que adquire dados relativos aos espectros de prótons, electrões e iões pesados. Conta o número de partículas detectadas num certo período de tempo e organiza-as em canais de energia. Neste trabalho foi desenvolvido um algoritmo para a determinação dos fluxos de prótons e electrões com base nos dados provenientes do detector e nas funções de resposta obtidas através de simulações Monte Carlo. Este algoritmo faz uso do método da estimativa da máxima verosimilhança, que ajusta uma lei de potência com parâmetros desconhecidos aos dados. Isto porque se parte do pressuposto de que os espectros do fluxo de partículas obedecem a uma lei de potência com um índice espectral negativo. Os fluxos obtidos foram utilizados para reconstruir os dados que os originaram; estes dados reconstruídos foram então comparados com os originais, dando uma melhor noção das potencialidades e limitações do método. Os fluxos determinados foram também comparados com resultados análogos obtidos através dos dados de GOES-15, um satélite também em GEO, em que foi empregue um método diferente de desconvolução (redes neuronais artificiais). No geral o método implementado neste trabalho funcionou relativamente bem para ambas as espécies de partículas analisadas, dando origem a resultados similares aos obtidos pelo GOES. A maior desvantagem desta abordagem é a assunção de uma lei de potência *a priori*, que força uma forma aos espectros que não é sempre a mais exacta em todos os instantes.

Palavras-chave: Multi-Functional Spectrometer, Método da Estimativa da Máxima Verosimilhança, Fluxo de prótons, Fluxo de electrões, GOES

Abstract

MFS is a spectrometer in GEO which acquires data regarding proton, electron and heavy ion particle fluxes. It counts the number of particles detected for a given time period and organizes them in energy channels. In this work an algorithm was developed to determine the fluxes of protons and electrons based of the detector's data and channels response functions obtained through Monte Carlo simulations. The developed algorithm uses a maximum likelihood estimate method, which fits the data with a power-law with unknown parameters. This was based of the assumption that the particle fluxes follow a power-law with a negative spectral index. The obtained fluxes were used to reconstruct the data that originated them; this reconstructed data was then compared with the original data, in order to get a better understanding of the method's strengths and limitations. The fluxes were also compared with the results obtained with data from GOES-15, an analogous satellite also in GEO, treated with a different unfolding method (artificial neural networks). Overall the method implemented worked reasonably well for both particle types analysed, originating results similar to those obtained from GOES. The major weakness of this approach is the assumption of a power-law *a priori*, which forces a shape that is not always the most accurate at all times into the flux spectra.

Keywords: Multi-Functional Spectrometer, Maximum likelihood estimate method, Proton flux, Electron flux, GOES

Contents

Acknowledgments	iii
Resumo	v
Abstract	vii
List of Tables	xi
List of Figures	xv
Acronyms	xvii
1 Introduction	1
1.1 MFS overview	3
1.1.1 MFS particle identification	4
1.1.2 In-flight data	6
1.1.3 Simulation and ground tests	7
1.1.4 MFS channels response functions	8
2 Radiation Environment in GEO	9
2.1 Galactic Cosmic Rays	9
2.2 Van Allen belts	10
2.3 Solar Energetic Particles	10
3 Methods for Data Analysis	13
3.1 MFS data access and channels response functions	13
3.2 Determination of a flux based on a detector's count-rate	15
3.2.1 Proton and electron flux estimate	15
3.3 Obtaining the proton and electron fluxes from MFS counts	16
3.3.1 Maximum likelihood estimate method	16
3.3.2 Proton and electron flux estimate and uncertainty	17
3.4 Reconstructing MFS channels counts from the determined fluxes	18
4 Results and Discussion	19
4.1 SEP event analysed from December 26 th 2013 to January 16 th 2014	19
4.1.1 Proton flux spectra	20
4.1.2 Electron flux spectra	30

4.1.3	MFS vs. GOES flux spectra	35
4.2	"Baseline" analysed from April 18 th to April 21 st 2014	40
4.2.1	MFS electron flux spectra results and comparison with GOES	41
5	Conclusions	47
	Bibliography	50

List of Tables

- 1.1 Types of upsets 3
- 1.2 MFS requirements 4
- 1.3 Proton energies tested 8
- 1.4 Electron energies tested 8

List of Figures

1.1	AlphaSat configuration	2
1.2	MFS model setup	3
1.3	MFS data schematic	5
1.4	LUT schematic	5
1.5	Proton fluxes for MFS and SREM at 46MeV	6
1.6	MFS geometry	7
1.7	MFS ground test data	7
2.1	GCR energy spectra	10
2.2	Fluxes of particles trapped in the radiation belt	11
2.3	Daily fluences of SEP protons	11
3.1	Proton response functions	14
3.2	Electron response functions	14
4.1	MFS SEP proton data for all channels	19
4.2	MFS SEP electron data for all channels	20
4.3	SEP proton flux from 32.4 MeV to 37.77 MeV	20
4.4	SEP proton flux from 37.77 MeV to 44.03 MeV	21
4.5	SEP proton flux from 44.03 MeV to 51.34 MeV	21
4.6	SEP proton flux from 51.34 MeV to 59.86 MeV	21
4.7	SEP proton flux from 59.86 MeV to 69.79 MeV	22
4.8	SEP proton flux from 69.79 MeV to 81.37 MeV	22
4.9	SEP proton flux from 81.37 MeV to 94.87 MeV	22
4.10	SEP proton flux from 94.87 MeV to 110.61 MeV	23
4.11	SEP proton flux from 110.61 MeV to 128.96 MeV	23
4.12	SEP proton flux from 128.96 MeV to 150.36 MeV	23
4.13	SEP proton flux from 150.36 MeV to 175.30 MeV	24
4.14	SEP proton flux from 175.30 MeV to 204.39 MeV	24
4.15	SEP proton flux k parameter	25
4.16	SEP proton flux α parameter	25
4.17	SEP proton flux k vs α parameter	26

4.18 SEP proton reconstructed vs measured data for channel 1	27
4.19 SEP proton reconstructed vs measured data for channel 2	27
4.20 SEP proton reconstructed vs measured data for channel 3	27
4.21 SEP proton reconstructed vs measured data for channel 4	28
4.22 SEP proton reconstructed vs measured data for channel 5	28
4.23 SEP proton reconstructed vs measured data for channel 6	28
4.24 SEP proton reconstructed vs measured data for channel 7	29
4.25 SEP proton reconstructed vs measured data for channel 8	29
4.26 SEP proton reconstructed vs measured data for channel 9	29
4.27 SEP proton reconstructed vs measured data for channel 10	30
4.28 SEP electron flux greater than 0.8 MeV	30
4.29 SEP electron flux greater than 2 MeV	30
4.30 SEP electron flux greater than 4 MeV	31
4.31 SEP electron flux k parameter	32
4.32 SEP electron flux α parameter	32
4.33 SEP electron flux k vs α parameter	32
4.34 SEP electron reconstructed vs measured data for channel 1	33
4.35 SEP electron reconstructed vs measured data for channel 2	33
4.36 SEP electron reconstructed vs measured data for channel 3	34
4.37 SEP electron reconstructed vs measured data for channel 4	34
4.38 SEP electron reconstructed vs measured data for channel 5	34
4.39 SEP electron reconstructed vs measured data for channel 6	35
4.40 SEP electron reconstructed vs measured data for channel 7	35
4.41 MFS vs GOES SEP proton flux of 6.5 MeV	36
4.42 MFS vs GOES SEP proton flux of 11.6 MeV	36
4.43 MFS vs GOES SEP proton flux of 30.6 MeV	37
4.44 MFS vs GOES SEP proton flux of 63.1 MeV	37
4.45 MFS vs GOES SEP proton flux of 165 MeV	37
4.46 MFS vs GOES SEP proton flux of 433 MeV	38
4.47 MFS vs GOES SEP electron flux greater than 0.8 MeV	39
4.48 MFS vs GOES SEP electron flux greater than 2 MeV	39
4.49 MFS vs GOES SEP electron flux greater than 4 MeV	39
4.50 MFS baseline proton data for all channels	40
4.51 MFS baseline electron data for all channels	41
4.52 MFS vs GOES baseline electron flux greater than 0.8 MeV	41
4.53 MFS vs GOES baseline electron flux greater than 2 MeV	42
4.54 MFS vs GOES baseline electron flux greater than 4 MeV	42
4.55 Baseline electron flux k parameter	43
4.56 Baseline electron flux α parameter	43

4.57 Baseline electron flux k vs α parameter	44
4.58 Baseline electron reconstructed vs measured data for channel 1	44
4.59 Baseline electron reconstructed vs measured data for channel 2	45
4.60 Baseline electron reconstructed vs measured data for channel 3	45

Acronyms

AEEF	Alphasat Environment and Effects Facility
CME	Coronal Mass Ejection
CTTB	Component Technology Test Bed
ESA	European Space Agency
GCR	Galactic Cosmic Rays
GEO	Geosynchronous Equatorial Orbit
GOES	Geostationary Operational Environmental Satellite
HI	Heavy Ions
IFDA	In-Flight Data Analysis
IMF	Interplanetary Magnetic Field
LIP	Laboratório de Instrumentação e Física Experimental de Partículas
LUT	Look-Up Table
MFS	Multi-Functional Spectrometer
NOAA	National Oceanic and Atmospheric Administration
PSI	Paul Scherrer Institute
SEP	Solar Energetic Particles
SVD	Single Value Decomposition

Chapter 1

Introduction

On July 25th 2013, the largest European Telecom satellite ever built, the AlphaSat, was launched into geostationary orbit. Its primary function is to expand a global mobile network, provided by Inmarsat, a UK based company. ESA partnered with Inmarsat for the commissioning of this satellite, which hosts four Technology Demonstration Payloads developed through ESA's Advanced Research in Telecommunications Systems (ARTES) programme.

One of these payloads, illustrated in figure 1.1, is the AlphaSat Environment Effects Facility (AEEF), also referred to as TDP8, which is responsible for monitoring and acquiring data about the effects of radiation in geostationary orbit on electronic components and solid-state materials. It is composed of two experiments: the Multi-Functional Spectrometer (MFS) and the Component Technology Test Bed (CTTB) [1] [2].

The MFS is a complex radiation monitor that detects and identifies protons, electrons and heavy ions and measures their corresponding energies. This information is compiled to create spectra of counted particles over time. Thus, it is possible to know, at all instants, what particles of which energies compose the radiation environment. These were measured for an energy range of 50 keV to 10 MeV for electrons, 4 MeV to 300 MeV for protons and for a Linear Energy Transfer of $15 \text{ MeV cm}^2/\text{mg}$ to $70 \text{ MeV cm}^2/\text{mg}$ for heavy ions.

The CTTB is composed of three experiments boards: the intra satellite optical link technology demonstration board, also referred to as Sistema de Interconexiones Ópticas para Satélites (SIOS), the GaN technology experiment and the Memory Test Board (MTB). Additionally, a package flight lot carrying radiation-sensing field-effect transistors, or RADFETs (ESAPMOS4) is also included in the CTTB. Each board has a RADFET to monitor the dose deposited by ionizing radiation with sensitivity of up to 85 mV/rad [4]. MFS and CTTB have been acquiring data in geostationary orbit since August 28th, 2013 [5].

There are mainly three radiation sources that affect devices in space: trapped radiation in a planet's magnetic field (known as Van Allen belts for the Earth's case), Galactic Cosmic Rays (GCR) and Solar Energetic Particles (SEP). Geostationary orbit is at an altitude of 35,786 kilometres above the Earth's equator (approximately 6 Earth radii), which lies in the magnetosphere. Here, at such altitudes, high-energy (0.1-10 MeV) electrons are trapped in the outer Van Allen radiation belt. GCR also strike satellites

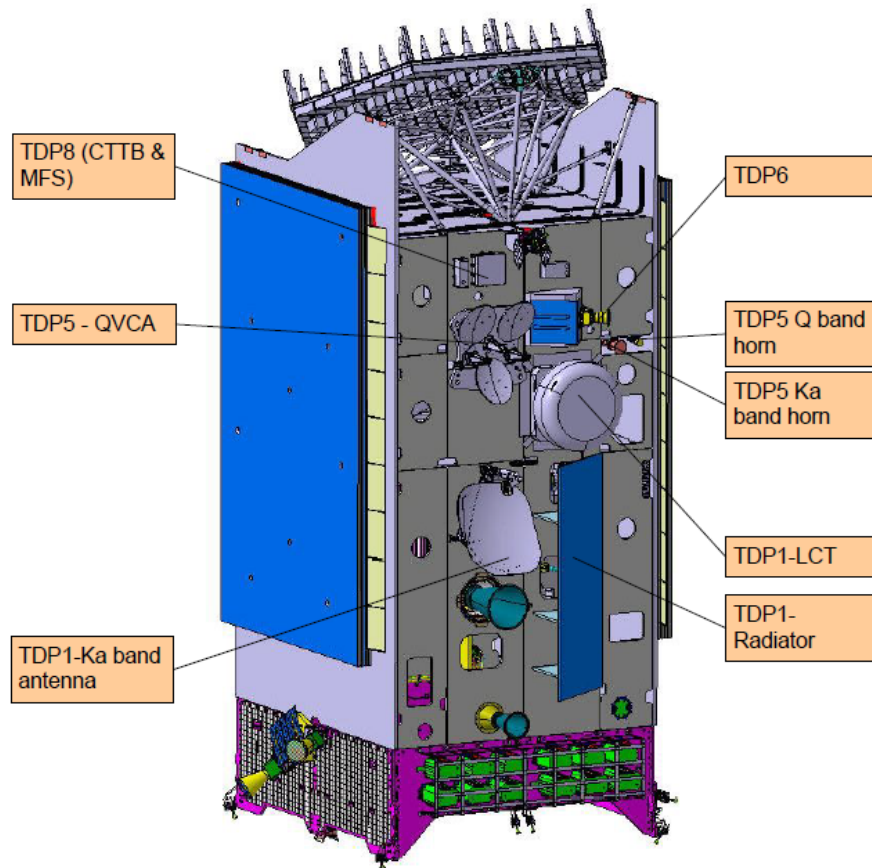


Figure 1.1: AlphaSat configuration. This work focuses on data acquired by TDP8 (CTTB & MFS). Taken from [3], Figure 2-1.

in GEO and consist mainly on protons (85%) and α -particles (14%). During solar events, SEP can also be observed in GEO, consisting on protons, electrons and heavy ions.

These particles, once they strike an electronic component, may cause several forms of upsets. Because they are ionizing particles, they might ionize the medium they are crossing, freeing electrons from the valence band of atoms into the conduction band, thus creating transient electric currents. These may change information stored, select an unwanted function, disrupt proper functioning or destroy a component. The holes created in certain regions of a device (like the Gate of a MOSFET) by the absence of electrons may also change its behaviour in the long run. Finally, non ionizing scattering of particles in a lattice can also be disruptive, because atoms might be removed from the lattice where they rest, resulting in long time degradation of the properties of the medium [6]. A summary of these upsets is presented in Table 1.1.

These upsets to electronic components (as well as damage to the human body) are the main concern with space radiation, that needs to be studied and characterized. This is what motivates the work in this thesis.

Specifically, the purpose of this work is to analyse data from MFS, namely to determine the fluxes of particles streaming through the detector based on its count-rates. To do this, a numerical method that unfolds the fluxes of protons and electrons was developed and implemented [7]. This method and its

Upset	Duration of upset	Effect on a component
Single-Event Upset	Transient	Data corruption/bit-flip
Single-Event Functional Interrupt	Transient	Unwanted function selection
Single-Event Latch-up	Until reboot	Functioning disruption
Single-Event Burnout	Permanent	Component destruction
Total Ionizing Dose	Long-term cumulative	Change in component behaviour
Displacement Damage	Long-term cumulative	Change in component behaviour

Table 1.1: Different forms of radiation induced upsets observed in electronic components.

implementation will be described in chapter 3. The results obtained as well as the method itself will be discussed and analysed in chapter 4.

1.1 MFS overview

The MFS is composed of a stack of eleven silicon detectors, with sizes varying from 50mm² to 900mm², interleaved by layers of absorber material (aluminium and tantalum), as well as a collimator made of tantalum, that allows the spectrometer to operate under high particle fluxes. It was designed to detect particles coming from a 35° angle field of view (FOV), so it also includes for this purpose a tantalum wall around the stacked detectors. This way signals coming from out of FOV particles, that would affect MFS' particle recognition process, could be avoided. A schematic of MFS is shown in figure 1.2.

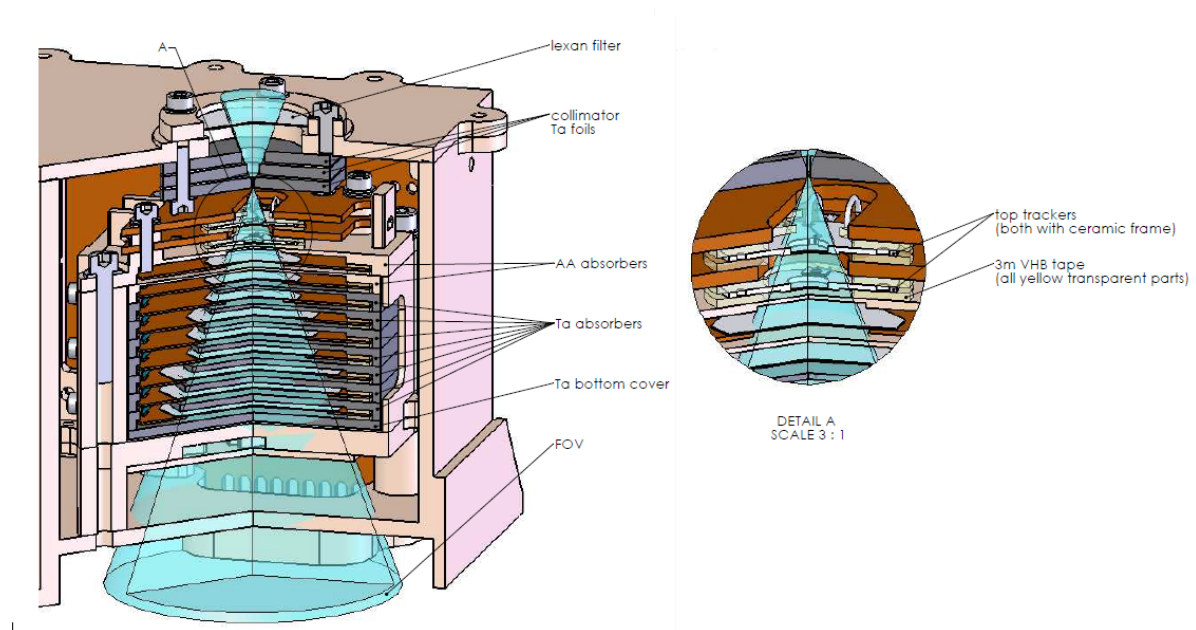


Figure 1.2: MFS geometrical schematic [8].

Once the particles hit MFS, they lose energy as they cross the layers of silicon detectors and absorber material. This energy loss is a known process, which for this experiment is validated through ground tests and computer simulations. The silicon detectors will send signals to the MFS Data Processing units, carrying information about the energy loss in each stack. With this information, and based on Look-Up Tables developed for this purpose (through ground tests and simulation), it is possible to identify

the particles that cross the detectors, as well as their energy [9]. The MFS technical capabilities are summarized below, in Table 1.2.

Description	Requirement
Electrons	450keV to 7MeV Energy resolution: < 20%
Protons	1MeV to 200MeV Energy resolution: < 10%
α -particles	5MeV to 200MeV Energy resolution: < 20%
Heavy Ions	5MeV/amu to 50MeV/amu Particle separation: 1 amu up to $Z = 8$
Count-Rate	$1 \times 10^7 (cm^{-2}s^{-1})$ for electrons or protons of energy > 1MeV
Field of view	35°
Accumulation time	60s to 600s in 60s steps
Power consumption	5W

Table 1.2: Main MFS requirements. Taken from [10], Table 3-5.

The MFS also contains three boards, besides its detectors: a frontend board, a backend board and a power supply board. The frontend board provides a first step in the signal analysis and processing. Analogue raw signals are provided by the detectors and the frontend board amplifies and digitalizes these signals into digital outputs (ADC channels). After this first treatment, the backend board receives the digital signals and processes them to identify the incoming particles and corresponding energies, which are associated with a given energy channel, that encompasses an energy interval. This board then provides as output the number of counts registered for each particle type and energy channel for each data acquisition time interval (typically around 60 seconds). It also has a veto algorithm system that excludes signals that are expected to not be representative of a true particle hit and are instead caused by some transient current or electronic noise. The backend board handles the state of the instrument, data storage and the communications with CTTB and Earth as well. Finally, the power supply board provides filtering of the power supplies and generates additional power supplies needed to operate MFS [10]. A schematic is shown in Figure 1.3.

1.1.1 MFS particle identification

The MFS particle identification process occurs in the backend board. When it receives digital inputs from the frontend board it searches for the plane with maximum deposited energy and checks if the first plane also registered deposited energy. If not, it means that the incoming particle didn't reach the detector through the collimator entrance (which would force it to go through all planes until it reached the maximum deposited energy one); it would instead mean that it penetrated the tantalum walls of the detector and is therefore not eligible as a "particle hit". When this happens the occurrence is vetoed and discarded.

If the system does not veto the event, it then finds and analyses the plane that registered the largest value of energy deposited. The algorithm then compares the signal with established thresholds that associate the event to a particle type. These thresholds were determined and fine-tuned from Monte

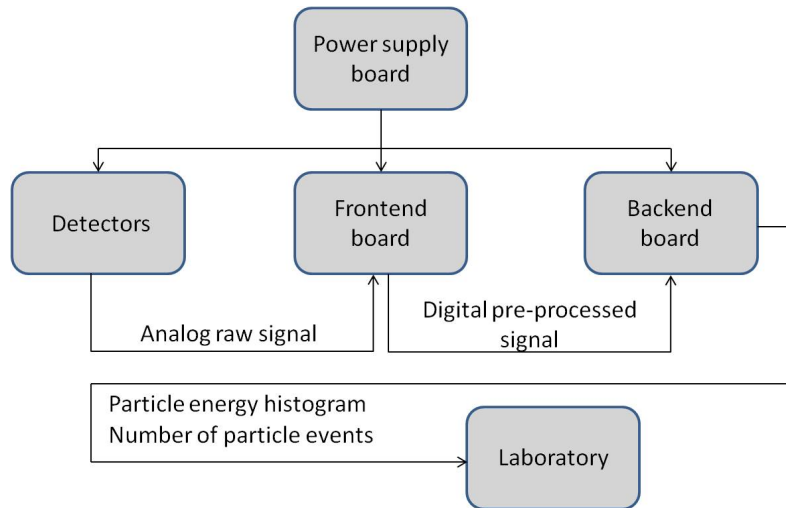


Figure 1.3: MFS data acquisition and processing schematic.

Carlo simulations and test beam data.

After identifying the incident particle, MFS determines its energy and associates it to a given energy channel. For this process to be done, besides the information on the particle identification, it's required the ID of the plane where most energy was deposited and the value of energy deposited on the plane immediately before. This information is stored in 16 bits which yield a number, that is contained in a Look-Up Table (LUT) that then associates it with an energy bin (channel).

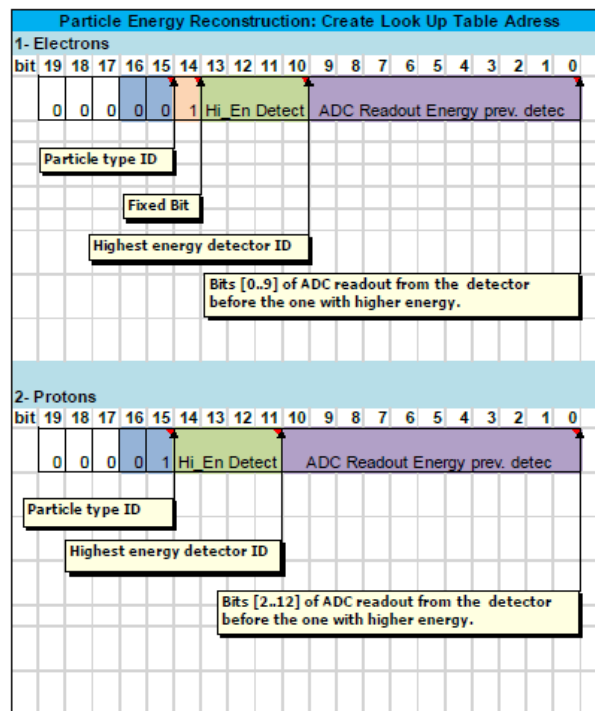


Figure 1.4: MFS energy reconstruction LUT schematic. Taken from [3], Figure 3-33.

As can be seen in figure 1.4, bits 15 and 16 have information on what particle was detected (00 for electrons, 01 for protons and 1x for α -particles and heavy ions); the next four bits identify the plane with most energy deposited (plane ID: 11 detector planes require 4 bits to be represented), except in

the case of electrons where bit 14 is a dummy bit with value set to 1; the remaining 10 and 11 bits for electrons and protons respectively are the readout from the frontend board's ADC regarding the detector plane that precedes the one with most energy deposited. The resulting number is then contained in an interval of the LUT which associates it to a specific channel [3].

1.1.2 In-flight data

To gather and organize data acquired, perform basic analysis, validate data and make it available via the internet, the *In-Flight Data Analysis* (IFDA) platform was developed by *EVOLEO Technologies* to store all relevant information and make it available online to the working groups [11]. The information required to elaborate this work was taken from this platform.

As explained, MFS data is recorded as a function of the energy of the primary particles (electrons, protons and HI) reaching the detector. For protons there are ten energy bins (channels) ranging between 11 MeV and 200 MeV and for electrons there are seven energy bins, ranging from 450 keV to 7 MeV. This information is obtained from IFDA in the form of histograms with particle counts per channel for around sixty seconds time intervals and it can be then used to extract proton and electron flux spectra as a function of time (see Figure 1.5).

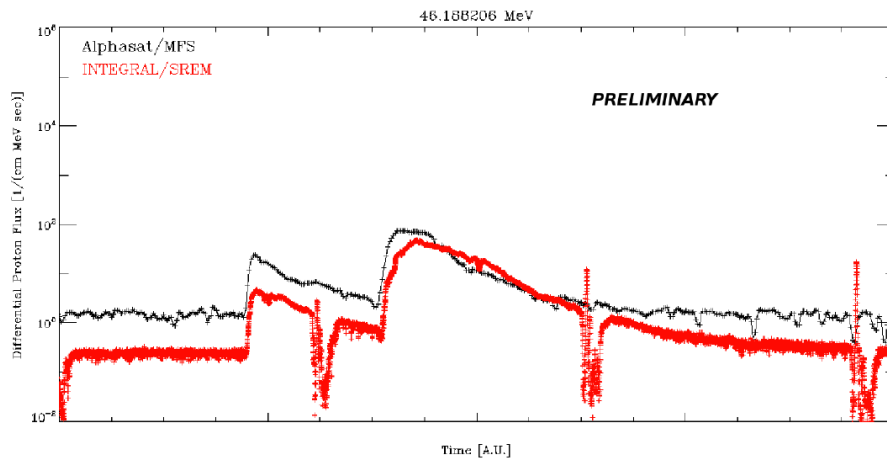


Figure 1.5: Differential proton flux series at $E \approx 46$ MeV, derived from data collected from MFS (dark crosses) and an equivalent ESA spectrometer: SREM (red crosses). Data collected from December 26th 2013 to January 17th 2014. Taken from [12], Figure 3.

In this figure, MFS data was used to determine the fluxes shown, which were also compared with analogous results for another experiment - SREM (Standard Radiation Environment Monitor) on board of ESA's INTEGRAL (INTErnational Gamma-Ray Astrophysics Laboratory) [13]. The method used in this case was a single value decomposition (SVD) method which is not the same as the one used in this work. This image is shown as an illustrative example of what this work aims to achieve; on a side note however, this satellite is not in GEO so its results will not be used for comparison in this work.

1.1.3 Simulation and ground tests

A detailed Monte Carlo simulation of MFS was implemented using the Geant4 simulator toolkit [3]. A model of the detector's geometry and materials that compose it was developed and tested for different incident particles (see Figure 1.6). This simulation was used to validate ground tests, performed at *Paul Scherrer Institute* (PSI), in Switzerland, in 2011. It was also used to characterize the detector's response functions to incoming particles, which are needed to predict the fluxes based on MFS count-rates.

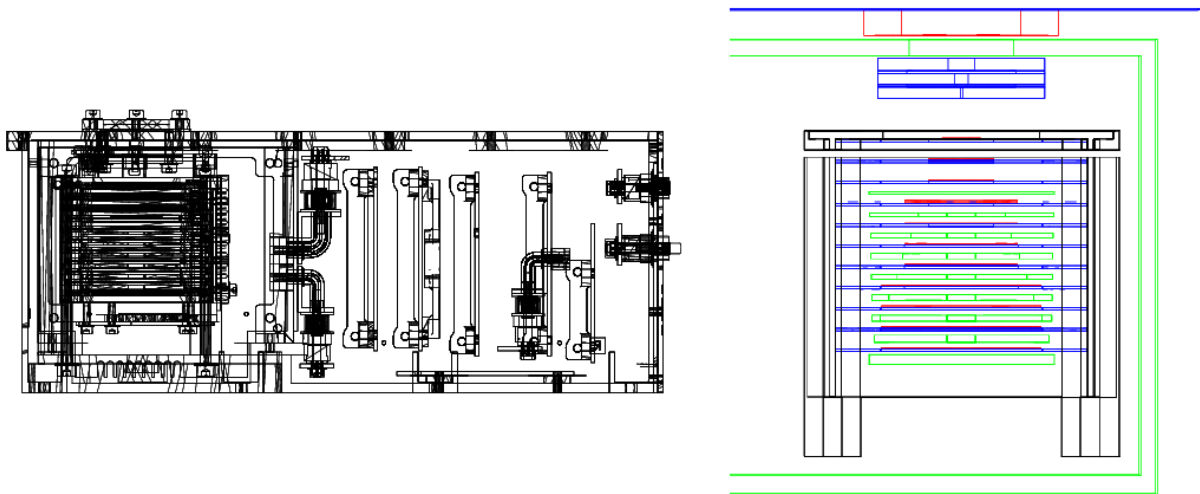


Figure 1.6: MFS schematic (on the left) and geometry used in the Monte Carlo simulation performed with Geant4 (on the right). Taken from [7], Figure 2 and [3], Figure 3-2, respectively.

One output of this simulation was histograms of counts of particles as a function of energy, converted in ADC channel outputs, as shown in Figure 1.7.

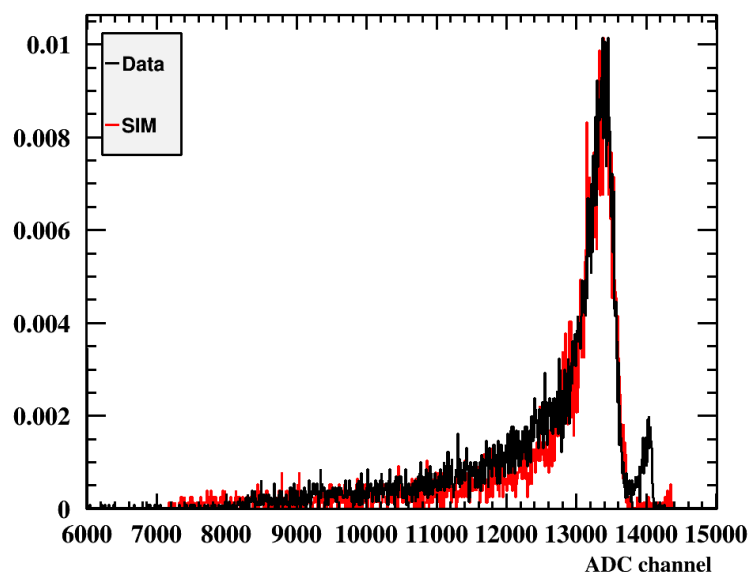


Figure 1.7: Data from a ground test and a simulation. It shows the count-rate of protons as a function of the energy lost (ADC channel relates to energy) on the first silicon layer of the MFS detector, for a proton beam of energies of 31.2MeV. Taken from [12], Figure 2.

These allowed the determination of the correct gain calibration to be applied in each plane of the stacked detectors. This calibration was done using proton beams of energies of 120.2 MeV, 134.8 MeV and 150.0 MeV by both simulation and tests. The tests and simulations included more proton energies (see Table 1.3), however only high energy protons can be used to calibrate all the layers of the detector, because low energy protons are absorbed in the first layers and therefore will not reach the last one, at the bottom of the stack.

Proton energies tested (MeV)	9.6	19.0	31.2	61.9	76.1	91.0	106.2	120.2	134.8	150.0
------------------------------	-----	------	------	------	------	------	-------	-------	-------	-------

Table 1.3: Proton beam nominal energies that were tested. Taken from [3], Table 3-2.

Electron beams were also used to test and simulate MFS response to these particles. The energies used are presented below:

Electron energies tested	300keV	600keV	900keV	1.1MeV	1.2MeV	1.5MeV	2.1MeV
--------------------------	--------	--------	--------	--------	--------	--------	--------

Table 1.4: Electron beam nominal energies that were tested. Taken from [3], Table 3-4.

Afterwards, data regarding incident protons and electrons gathered from simulations was compared with corresponding data from ground tests, as shown in Figure 1.7. The simulation results are globally in good agreement with the measurements performed at PSI. The MFS particle identification and energy reconstruction algorithms were also tested [10].

1.1.4 MFS channels response functions

To quantify each channel's sensitivity to incoming particles and corresponding energies, simulations of omnidirectional protons (with energies ranging from 0MeV to 200MeV) and electrons (with energies ranging from 0MeV to 5MeV), were made, impacting uniformly over MFS top and lateral surfaces. Particles impacting on the bottom surface were not generated, because of the AlphaSat shadow effect: the natural shielding the satellite provides to MFS prevents particles from reaching the detector. The purpose of these simulations is to obtain the ratio between detected and generated particles for each energy channel, for a given surface area and solid angle. These ratios are a measurement of each channel's efficiency to each incoming particle type and corresponding primary energy.

Particles lose energy as they cross the medium, namely the stack of silicon detectors and absorbers, and this is quantified by the simulation. Using this information combined with the expected behaviour of MFS electronics and signal processing units, one can determine the expected outcome of the whole MFS detection process for a certain (controlled) particle input. This information is presented as the MFS geometrical efficiency, expressed in units of $cm^2 sr$, as a function of a particle's energy, for each particle, in each response function. MFS response functions are presented further ahead in chapter 3, figures 3.1 and 3.2.

Chapter 2

Radiation Environment in GEO

It is important in the context of this work to understand the radiation environment to which MFS is subjected. This allows us to know what to expect and to analyse the obtained results in light of the current knowledge regarding space radiation.

First and foremost it should be referred that solar activity is not only a source of space radiation, but that it also affects and modulates other sources. It follows a cycle that is approximately 11 years long: for about 7 years activity levels are high, which are referred to as a solar maximum period; and for the remaining 4 years activity levels are low, referred to as a solar minimum period [14].

At GEO altitude (~ 5.6 Earth radii above the equator) there are three sources of radiation: Galactic Cosmic Rays (GCR), charged particles trapped in Earth's magnetic field and radiation resulting from solar activity. The first is a somewhat steady flux of charged particles that varies with the solar cycle; the second is the result of charged particles being trapped by Earth's magnetic field forming belts, also known as Van Allen belts; the third consists on plasma being expelled by the sun and reaching Earth. A brief description of each of these phenomena is given in the next sections.

2.1 Galactic Cosmic Rays

GCRs are high energy charge particles that originate from outside the solar system and consist mainly on protons (87%) and α -particles (12%), with residual contribution from heavier ions (1%), with energies that can reach up to 10^{11} GeV [14]. GCR fluxes vary inversely to the the solar cycle, i.e. GCR fluxes are lower during the solar maximum and higher during the solar minimum, for energies smaller than $\sim 10^4$ MeV. This is because during the solar maximum there is more solar activity that affect the interplanetary magnetic field (IMF), deflecting lower energy GCRs. Figure 2.1 shows the relation between the solar cycle and GCR fluence for different energies.

Protons with an energy < 200 MeV, which is the energy range required for MFS (see table 1.2), have a flux that ranges between $\sim 0.1 s^{-1} MeV^{-1} sr^{-1} m^{-2}$ and $\sim 1 s^{-1} MeV^{-1} sr^{-1} m^{-2}$. In this work the unit used to express flux (see equation 3.3) is $s^{-1} MeV^{-1} sr^{-1} cm^{-2}$, which means that MFS is subjected to proton fluxes originated from GCR between $\sim 10^{-5}$ and $\sim 10^{-4} s^{-1} MeV^{-1} sr^{-1} cm^{-2}$.

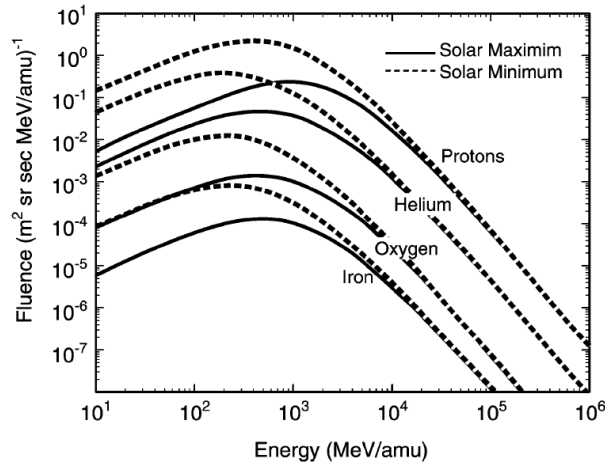


Figure 2.1: GCR energy spectra for several elements. Taken from [14], Figure 5.

2.2 Van Allen belts

Earth's magnetic field behaves approximately as a dipole with a north and south pole. This field would extend to infinity, getting weaker along the distance to its source if space was a vacuum. However, plasma emitted by the sun, referred to as "solar wind", is composed of moving charged particles which induce a magnetic field and reach Earth. This compresses the magnetic field of our planet on the dayside to roughly 10 Earth's radii and stretches it on the nightside to hundreds of Earth's radii [15]. The region where the dominant magnetic field is the one produced by Earth is the magnetosphere.

In the magnetosphere, Earth's field traps charged particles, forming radiation belts, known as Van Allen belts. These are well defined and constant over time in the region closest to Earth (the inner belt, that extends up to 2.7 Earth radii); however on the outer region further away from the planet (the outer radiation belt, that extends up to 10 Earth radii) they are not so well defined and change in time because they are affected by solar wind [14]. Particle fluxes on these belts based on models developed by NASA are shown in figure 2.2.

There can be seen the trapped protons and electrons on the referred belts. Protons have larger mass than electrons so they need a stronger magnetic field to be contained and exist mostly in the inner region of the magnetosphere, with energies ranging from 1 keV to 300 MeV. Electrons extend to the extremities of the magnetosphere, with energies ranging from 1 keV to 10 MeV [14].

So at GEO altitude, concerning Van Allen belts, only trapped electrons make relevant contributions to the radiation environment. Here, solar wind can disturb Earth's magnetic field and affect electron density, making it larger on the dayside and smaller on the nightside, as will be seen in this work in chapter 4.

2.3 Solar Energetic Particles

There are two categories of solar particle events, or SEPs, that make up the solar wind: solar flares and coronal mass ejections (CMEs). Solar flares are originated by a burst of energy released by the Sun's

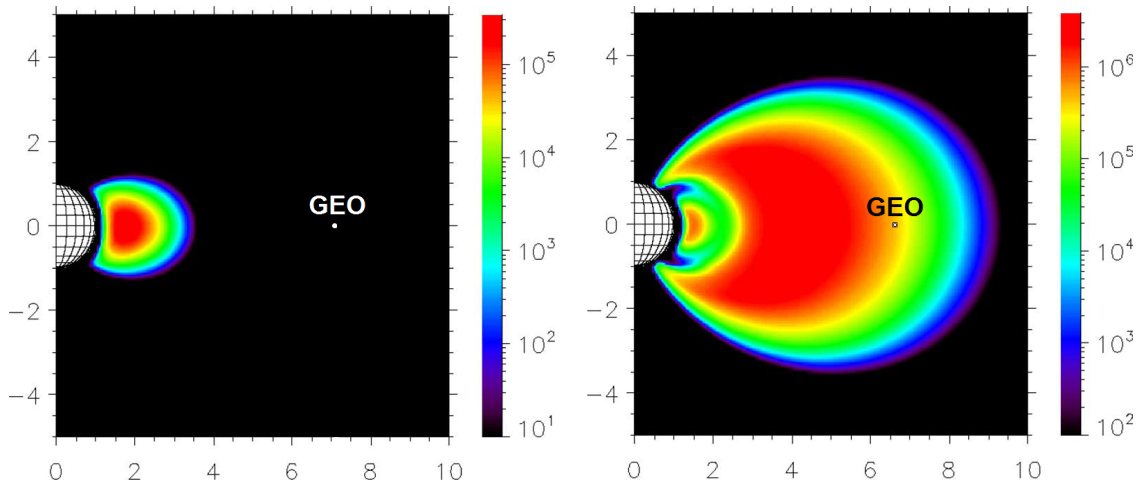


Figure 2.2: On the left: omnidirectional integrated proton fluxes ($cm^{-2}s^{-1}$) trapped in the radiation belt from NASA AP8 max model (energy >10 MeV). On the right: omnidirectional integrated electron fluxes ($cm^{-2}s^{-1}$) trapped in the radiation belt from NASA AE8 max model (energy >1 MeV). The mapping is done in magnetic coordinates given here in earth radii. Adapted from [14], Figure 28.

magnetic field and are rich in electromagnetic radiation and electrons [14]. They travel at high speeds and can last for hours, impacting the Earth's atmosphere shortly after being released. On the other hand, a CME is a slower eruption of plasma that can take days to reach Earth, moves as a shockwave and carries a large mass of charged particles (10^9 to 10^{11} tons), around 96% of which are protons [14]. It also carries an embedded magnetic field that can be stronger than the background interplanetary magnetic field associated with solar wind [16]. Because of this a CME can disturb the magnetosphere of Earth, causing geomagnetic storms. These can be quite upsetting to satellites in GEO because they can compress the magnetosphere, moving the magnetopause (the border between the magnetosphere and the IMF) beyond GEO orbit. This increases the exposure of satellites to the incoming large fluxes of high energy SEP protons and heavy ions. Both solar flares and CMEs (and therefore SEPs) are more frequent during the solar maximum (see figure 2.3).

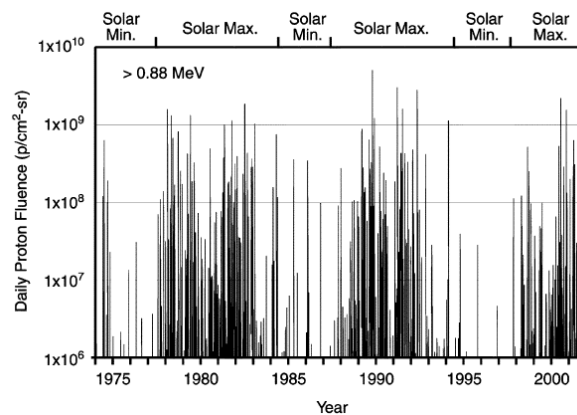


Figure 2.3: Daily fluences of >0.88 MeV protons due to solar particle events between approximately 1974 and 2002. Taken from [14], Figure 10.

Chapter 3

Methods for Data Analysis

3.1 MFS data access and channels response functions

MFS in-flight data is gathered and made available at IFDA, as previously stated. This data is presented in a *comma-separated values* (.csv) file, for a given time period. Data is displayed in nine columns (for electrons) or in twelve columns (for protons): date (dd/mm/yyyy), time (hh:mm:ss) and registered counts for each of the seven (electron) or ten (proton) MFS channels, between consecutive times. For analysis purposes, the data was saved into text files (.txt), where the date and time were converted into the accumulated time, in seconds, after the first measurement and unrealistically high counts (probably due to current peaks/electronic noise) were discarded. This allowed the data analysis process to be simpler and more convenient. On a qualitative level however, it is more advantageous to analyse plotted graphs, such as the ones shown in figures 4.1 and 4.2.

As described before in this work's introduction, simulations of omnidirectional protons and electrons to quantify MFS response to incoming particles were made. The results of these simulations were the MFS response functions.

A Root (.root) [17] file was therefore generated for each type of MFS channels (protons and electrons), containing histograms for each channel's energy response to each type of incoming particles. These histograms are used to determine particle fluxes, since they give the relationship between the counts registered by each channel and the flux that originated them. Only protons and electrons were analysed, because they are the most common particles present in GEO altitude. Plots of proton and electron channels response functions to incoming protons and electrons, respectively, are shown in figures 3.1 and 3.2.

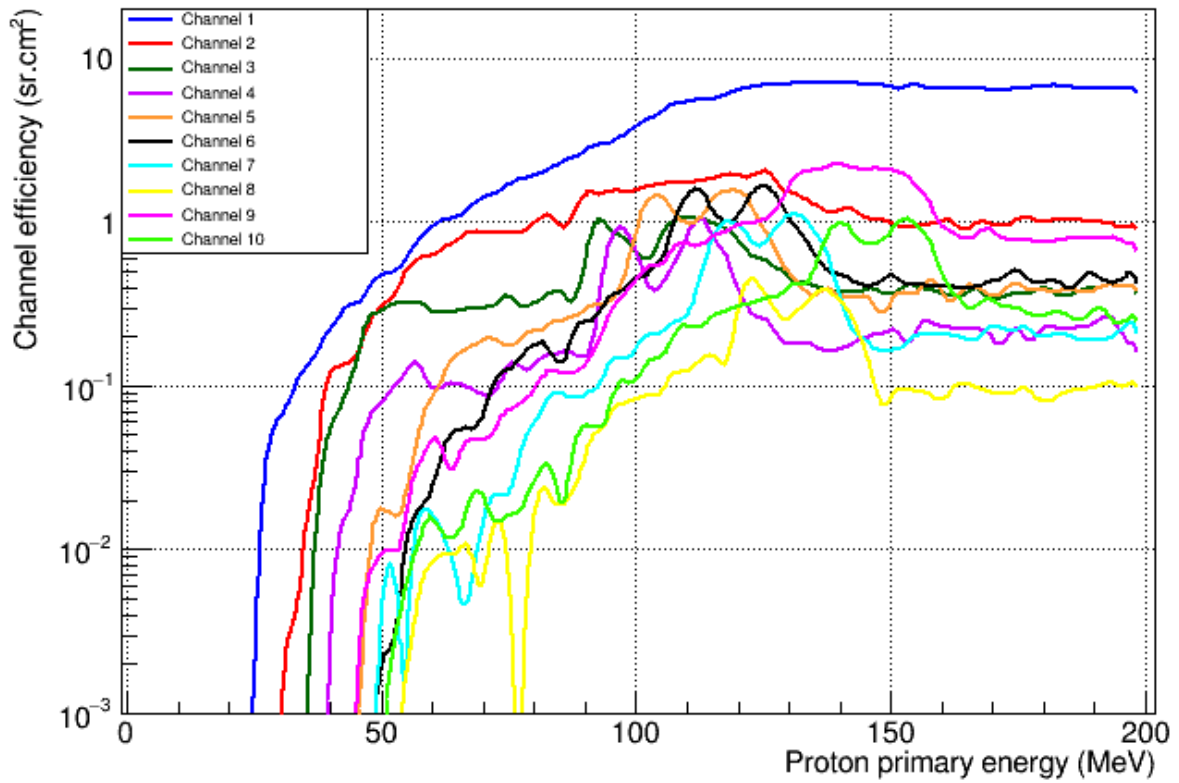


Figure 3.1: Proton channels response functions to incoming protons.

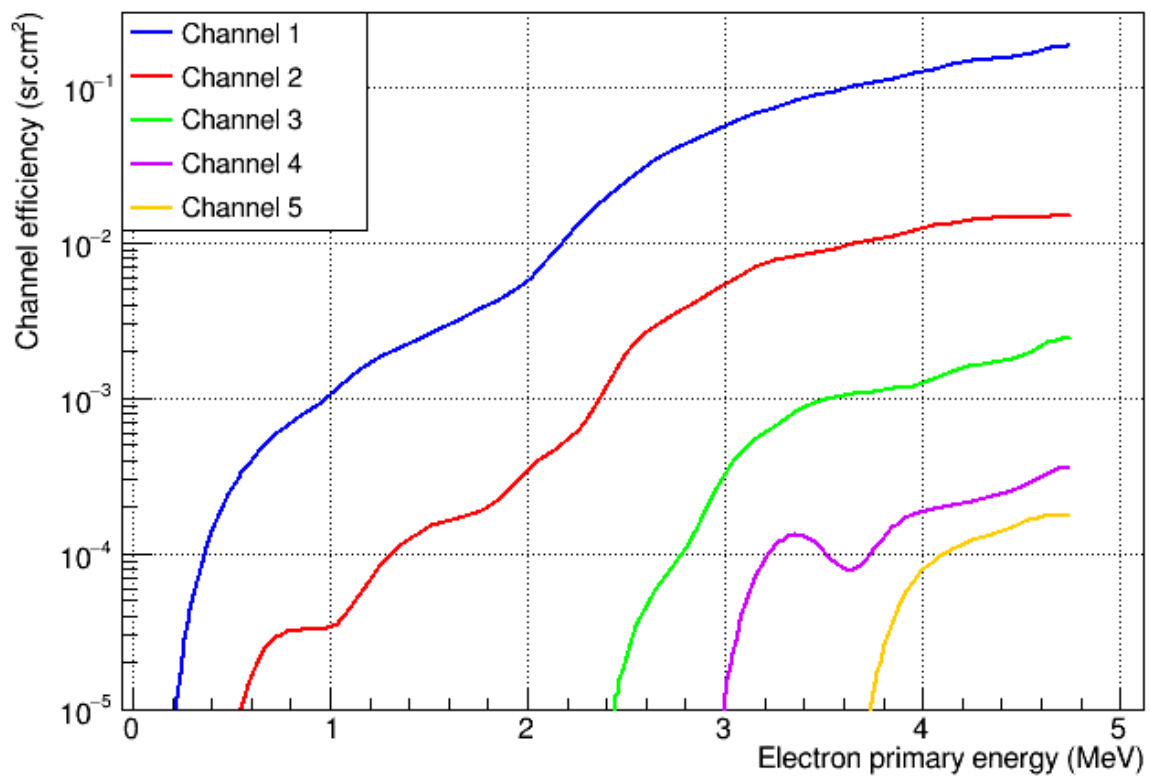


Figure 3.2: Electron channels response functions to incoming electrons. Channels 6 and 7 did not acquire statistically relevant data and are therefore not shown.

As can be seen in the electron channels case, several response functions adopt a value of zero $sr.cm^2$ for some energy intervals. Channels 6 and 7 do not seem to have any sensitivity to incoming electrons up to 5 MeV. This was problematic for the developed method to work properly because it had issues computing the number zero which was the value of several bins of the response functions (and of virtually all the bins of channels 6 and 7). To go around this problem a baseline value of $10^{-7} sr.cm^2$ was added to all bins of the electron response functions. This value was decided on inspection of the response functions and was determined to be small enough to not affect results while allowing for the algorithm used to converge on a solution. This process will be explained in the next sections: how the response functions were quantitatively used in the determination of the fluxes.

3.2 Determination of a flux based on a detector's count-rate

In general, a detector's count-rate can be expressed in the following way [18]:

$$C(x, t_0) = \frac{1}{T} \int_{t_0}^{t_0+T} dt \int_S d\sigma \cdot \hat{r} \int_{\Omega} d\omega \int_0^{\infty} dE \times \sum_{\alpha} \epsilon_{\alpha}(E, \sigma, \omega, t) \Phi_{\alpha}(E, \omega, x, t), \quad (3.1)$$

where $\int_{t_0}^{t_0+T} dt$ is the integral over time, $\int_{\Omega} d\omega$ is the integral over solid angle, $\int_S d\sigma \cdot \hat{r}$ is the integral over the sensitive area of the telescope, $\int_0^{\infty} dE$ is the integral over incoming particle energies, \sum_{α} is the sum of the contributions of each particle type. $\epsilon_{\alpha}(E, \sigma, \omega, t)$ is the detector's efficiency to a certain particle's energy, for a given sensitive area, solid angle and acquisition time, and $\Phi_{\alpha}(E, \omega, x, t)$ is the particle's flux, corresponding to a certain energy, solid angle, spatial orientation and moment in time.

In this context, it shall be assumed that:

- the particle fluxes are isotropic, dropping their spatial (x) and directional (ω) dependency;
- the particle fluxes are constant for each of the considered time intervals ($\int_{t_0}^{t_0+T} dt = \Delta t$).

The detector's efficiency $\epsilon_{\alpha}(E, \sigma, \omega)$ is quantified by the response functions obtained through numerical simulation. So it contains, for each incoming particle's energy, information regarding the detector's sensitive area and solid angle - there is one response function for each MFS channel and particle type [12]. So the general case presented in 3.1 can be written as:

$$C = \Delta t \int_{\Delta E} \sum_{\alpha} F_{R_{\alpha}} \cdot \Phi_{\alpha}(E) dE. \quad (3.2)$$

In this equation, C represents the total number of particles counted by a given MFS channel, $F_{R_{\alpha}}$ is the channel's response function to particle ' α ' and Φ_{α} is that particle's flux. Here, F_R has units of $cm^2 sr$ and so Φ is expressed in terms of $cm^{-2} MeV^{-1} sr^{-1} s^{-1}$ units.

3.2.1 Proton and electron flux estimate

According to [19] the flux of incoming particles from the sun can be described by an expression such as

$$\Phi(E) = kE^{-\alpha}, \quad (3.3)$$

where α is the flux's spectral index and k is a scale factor, representing the flux of 1 MeV incoming particles: $\Phi(E = 1MeV) = k$.

So for an incoming particle type such as protons the problem is simplified to:

$$C = \Delta t \int_{0MeV}^{200MeV} F_{R_{pp}} \cdot \Phi_p(E) dE, \quad (3.4)$$

where C are the count measurements from an MFS protons channel, during a time period Δt and $F_{R_{pp}}$ is that channel's response function (evaluated from 0MeV to 200MeV) to the incoming protons. $\Phi_p(E)$ is the proton's flux, described by 3.3. It has only energy dependency because of the assumptions previously made.

Analogously for electrons:

$$C = \Delta t \int_{0MeV}^{5MeV} F_{R_{ee}} \cdot \Phi_e(E) dE. \quad (3.5)$$

Here $F_{R_{ee}}$ is a given MFS electrons channel's response function to incoming electrons. These response functions were simulated to incoming electrons with an energy range of 0MeV to 5MeV.

3.3 Obtaining the proton and electron fluxes from MFS counts

The only unknown variable in equation 3.2 is $\Phi_\alpha(E)$. The unknown parameters in these equations are k and α , which depend on the measured counts for a given time period. Using a maximum likelihood estimate method to compare and fit the measured counts with the expected counts yielded by the parameters, for a given MFS channel, we can determine the best values for the referred parameters. This method is implemented using root's *TMinuit* minimization tool, allowing for an efficient and robust estimation of the parameters and corresponding uncertainties [20]. There are several minimization methods available in *TMinuit* tool. The one that was used is called *MIGRAD* and it's the standard method used for most cases. A more detailed explanation on how the maximum likelihood estimate method is applied to fit the data is given below.

3.3.1 Maximum likelihood estimate method

Since the number of counts registered by the several MFS channels, for a given time period, are integers independent from one another and can take small values (< 10 counts), the channels counts follow a Poisson distribution:

$$P(X = x) = \frac{\lambda^x e^{-\lambda}}{x!}, \quad (3.6)$$

where in this context the variable x represents the counts from a certain MFS channel and λ is their

average number. We want to discover in the function 3.4 the unknown parameters that allow the best value of λ , for each dataset of x , to be obtained, thus $\lambda = \Delta t \int F_R.kE^{-\alpha}dE$. So the goal is to find the best pair (k, α) that generates the value of λ most adequate to all the counts obtained from the various MFS channels (n channels: ten for protons, seven for electrons), for a given time interval. So we obtain the following equation:

$$f(C|k, \alpha) = \frac{1}{C!} \left(\Delta t \int F_R.kE^{-\alpha}dE \right)^C e^{-\Delta t \int F_R.kE^{-\alpha}dE}, \quad (3.7)$$

which is the function in 3.6 applied to this situation in particular. The maximum likelihood estimate consists on writing the likelihood function and maximize it within the parameter space [21]:

$$L(k, \alpha|C) = \prod_{i=1}^n f(C_i|k, \alpha). \quad (3.8)$$

It is more convenient to work with the logarithm of the likelihood function, which turns the product into a sum:

$$\log L(k, \alpha|C) = \sum_{i=1}^n \left[C_i \log \left(\Delta t \int F_{R_i}.kE^{-\alpha}dE \right) - \Delta t \int F_{R_i}.kE^{-\alpha}dE - \log(C_i!) \right]. \quad (3.9)$$

Since we are only interested in maximizing the above expression regarding the k and α parameters, we can ignore the terms that do not depend on them. So it is only needed to maximize the following expression:

$$\sum_{i=1}^n \left[C_i \log \left(\int F_{R_i}.kE^{-\alpha}dE \right) - \Delta t \int F_{R_i}.kE^{-\alpha}dE \right]. \quad (3.10)$$

Here, the integrals $\int F_{R_i}.kE^{-\alpha}dE$ are integrated over the domain of the response function.

The best estimate of the parameters k and α are the ones that maximize equation 3.9 (or 3.10). Since most available tools are optimized to perform minimizations, we shall take the symmetric value of the likelihood function and find its minimum. This is the part of the process done using Root's *TMinuit* optimization tool.

3.3.2 Proton and electron flux estimate and uncertainty

Once the maximum likelihood estimate method implemented converges, all information regarding the proton or electron flux, for the considered time interval, is known, i.e. the value of the (differential) flux for each point in energy can be computed. Usually the flux is either expressed in its differential form - keeping its units of $s^{-1}sr^{-1}cm^{-2}MeV^{-1}$ - or as an integrated flux - having units of $s^{-1}sr^{-1}cm^{-2}$ - over a certain energy interval.

When dealing with the differential flux, since the parameters k and α are known, we simply use equation 3.3. Naturally, if we want to work with its integrated form, over a considered energy interval (say, from E_1 to E_2), the integral flux is computed as:

$$\Phi = \int_{E_1}^{E_2} kE^{-\alpha} dE. \quad (3.11)$$

These fluxes have an uncertainty associated with them, because the minimization parameters which are obtained from MFS counts also have associated statistical uncertainties. Root's TMinuit tool uses the latter to calculate each parameter's uncertainty, which can then be accessed by the user. With these it is possible to propagate the uncertainty of each parameter to obtain the final flux uncertainty (differential or integrated from E_1 to E_2). The formula used to propagate the errors is the variance formula: $s_f = \sqrt{\sum_i \left(\frac{\partial f}{\partial x_i}\right)^2 s_{x_i}^2}$, where s_f is the standard deviation of f and s_{x_i} is the standard deviation of each variable x_i .

So the error expression for the flux is

$$s_\Phi = \sqrt{\left(\frac{\partial \Phi}{\partial k}\right)^2 s_k^2 + \left(\frac{\partial \Phi}{\partial \alpha}\right)^2 s_\alpha^2}, \text{ where} \quad (3.12)$$

$$\begin{cases} \frac{\partial \Phi}{\partial k} = E^{-\alpha} \\ \frac{\partial \Phi}{\partial \alpha} = -kE^{-\alpha} \ln(E) \end{cases}, \text{ for the differential flux, or}$$

$$\begin{cases} \frac{\partial \Phi}{\partial k} = \frac{E_2^{1-\alpha} - E_1^{1-\alpha}}{1-\alpha} \\ \frac{\partial \Phi}{\partial \alpha} = \int_{E_1}^{E_2} -kE^{-\alpha} \ln(E) dE \end{cases}, \text{ for the integral flux, integrated from } E_1 \text{ to } E_2.$$

So from equations 3.3 or 3.11 and 3.12 we can obtain the estimate of $\Phi \pm s_\Phi$, for a given time Δt .

3.4 Reconstructing MFS channels counts from the determined fluxes

To better validate the method and obtained fluxes, virtual (reconstructed) counts were calculated. This is essentially the inverse process of the maximum likelihood estimate method: to calculate each channel's counts from the now obtained flux parameters. So far, in equation 3.2, C was known from MFS and $\Phi_\alpha(E)$ was unknown. Now, from the known $\Phi_\alpha(E)$, C can be calculated. Ideally, the reconstructed counts would be equal to the measured ones. This would never be the case as will be seen in chapter 4, because the method discussed fits a power-law to the data (which has some degree of randomness in its distribution). From a fit one can only obtain "the best" set of points that predicts the observed data behaviour and not a specific random sample, so deviations from the reconstructed data to the measured one are to be expected.

It should be stated that this method uses the exact time intervals provided by MFS data, i.e. the fluxes (and consequently the reconstructed counts) are determined based on the number of counts measured by the detector for an acquisition time of around 60 seconds. In other words, no rebinning was performed, so the reconstructed counts can be compared with raw data (as will be shown in chapter 4).

Chapter 4

Results and Discussion

The application of the maximum likelihood method to MFS data yielded proton and electron flux spectra for different energy intervals or points. In this chapter those results will be presented, analysed and compared with analogous results from GOES-15 satellite.

4.1 SEP event analysed from December 26th 2013 to January 16th 2014

MFS has been acquiring data since 2013 and one time interval that was analysed ranges from December 26th 2013 to January 16th 2014, because a moderate intensity SEP was observed during this period [22].

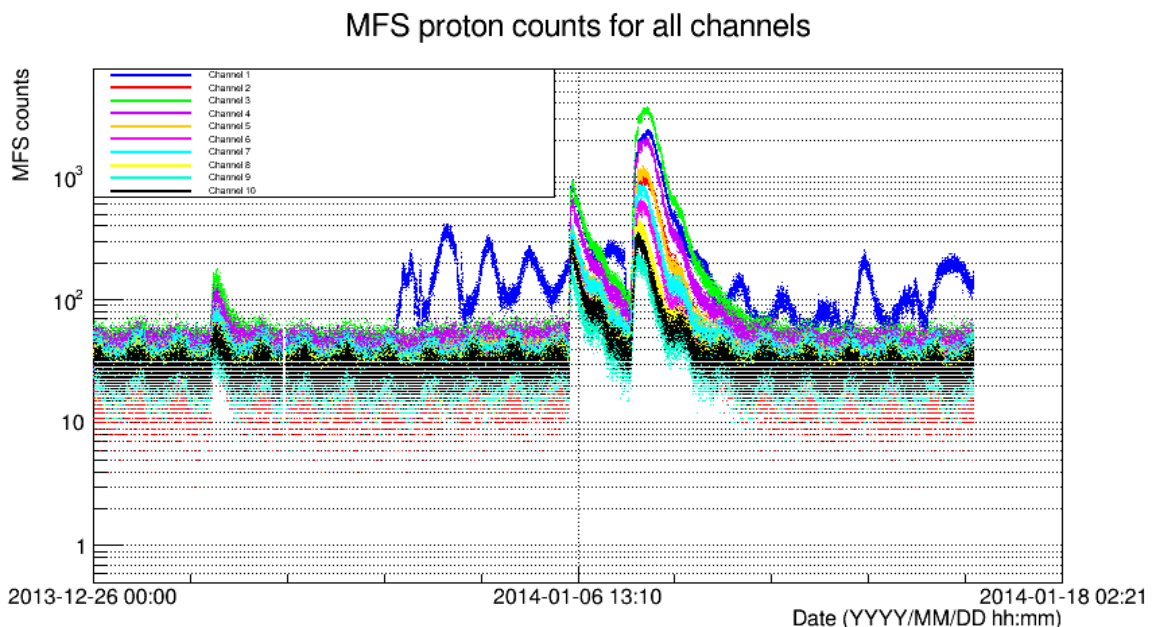


Figure 4.1: Data acquired by each MFS proton channel, starting at 26/12/2013 and ending at 16/12/2014.

These graphs show how many counts each channel registered for each 60 second time interval, plot-

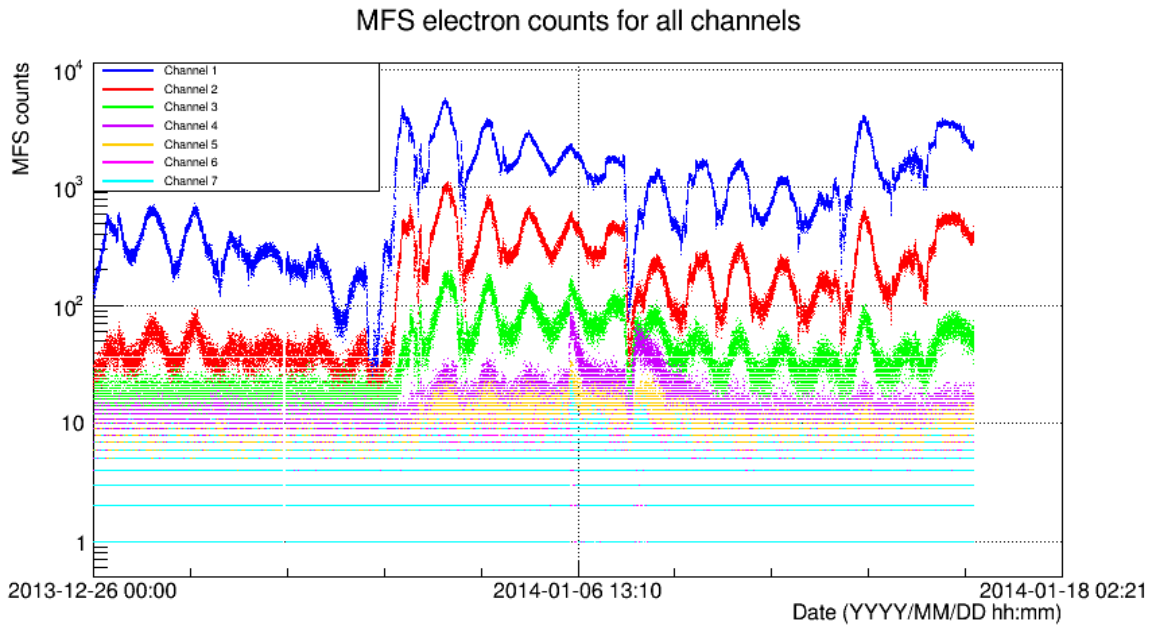


Figure 4.2: Data acquired by each MFS electron channel, starting at 26/12/2013 and ending at 16/12/2014.

ted over the twenty one days analysed. By use of the maximum likelihood estimate method developed in this work, proton and electron fluxes were produced from this data.

4.1.1 Proton flux spectra

Below are presented the obtained proton fluxes, on figures 4.3 through 4.14. These plots have the flux represented with green dots, with red error bars. Although they may seem that way, these are not asymmetric, as the graphs are plotted in logarithmic scale. The flux is presented in its integrated form, as show in equation 3.11.

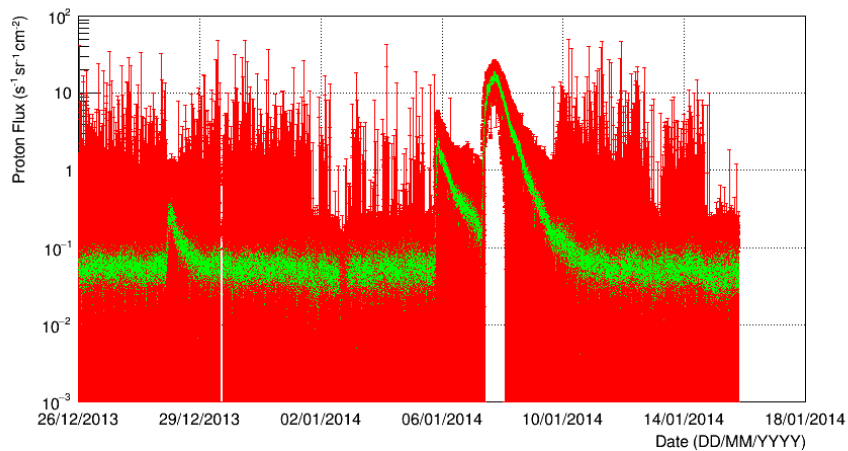


Figure 4.3: MFS proton flux spectra from 26/12/13 to 16/01/14, of energies between 32.40 MeV and 37.77 MeV.

These spectra have essentially three peaks in common. A smaller one around 29/12/2014, another

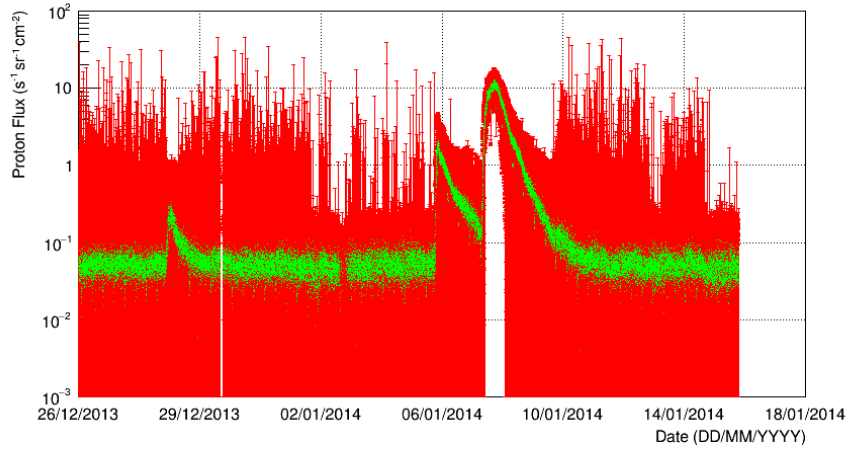


Figure 4.4: MFS proton flux spectra from 26/12/13 to 16/01/14, of energies between 37.77 MeV and 44.03 MeV.

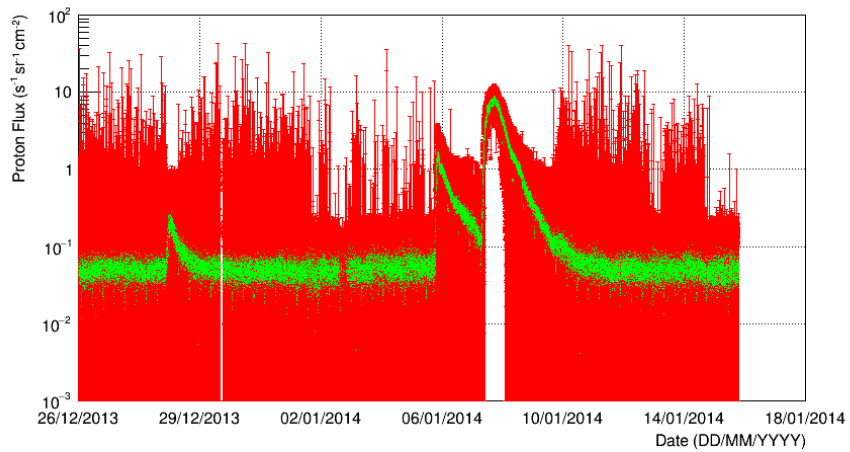


Figure 4.5: MFS proton flux spectra from 26/12/13 to 16/01/14, of energies between 44.03 MeV and 51.34 MeV.

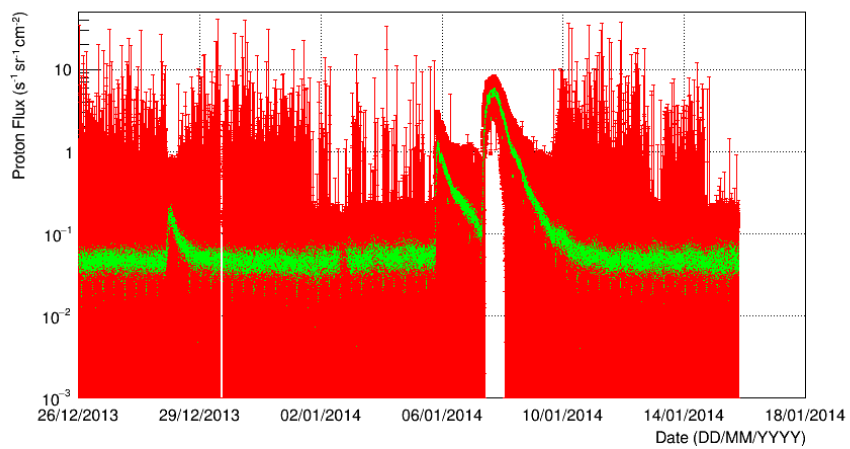


Figure 4.6: MFS proton flux spectra from 26/12/13 to 16/01/14, of energies between 51.34 MeV and 59.86 MeV.

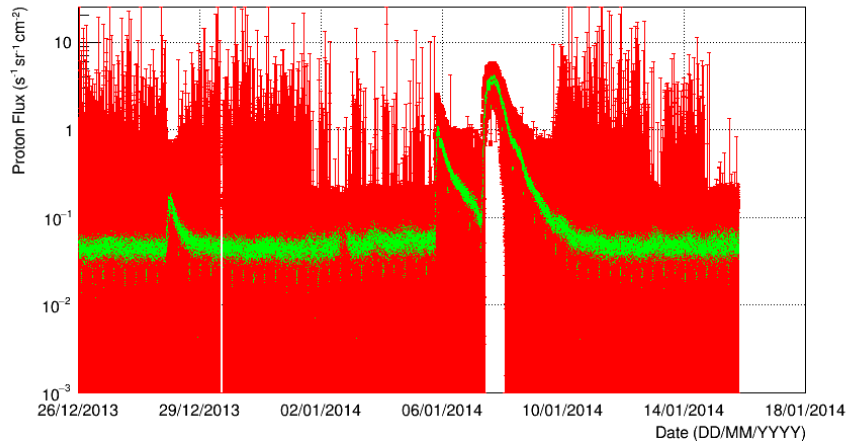


Figure 4.7: MFS proton flux spectra from 26/12/13 to 16/01/14, of energies between 59.86 MeV and 69.79 MeV.

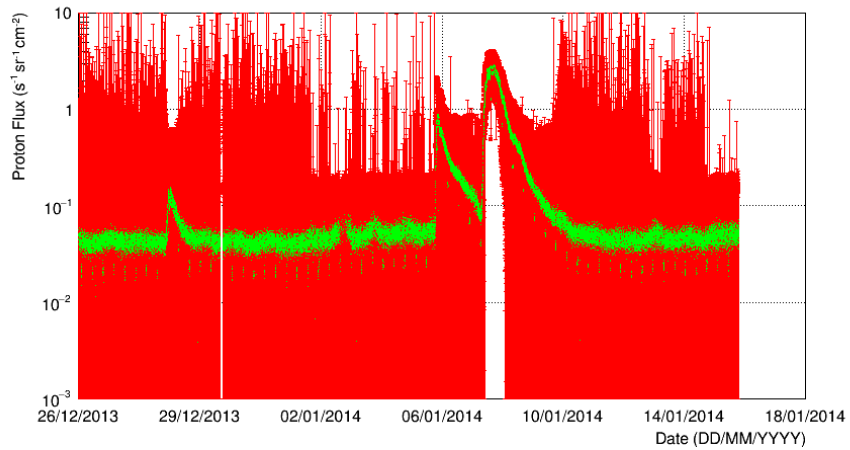


Figure 4.8: MFS proton flux spectra from 26/12/13 to 16/01/14, of energies between 69.79 MeV and 81.37 MeV.

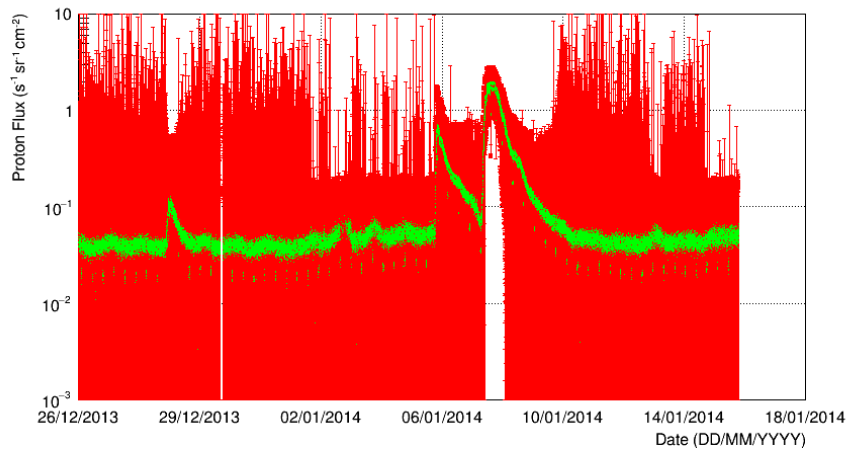


Figure 4.9: MFS proton flux spectra from 26/12/13 to 16/01/14, of energies between 81.37 MeV and 94.87 MeV.

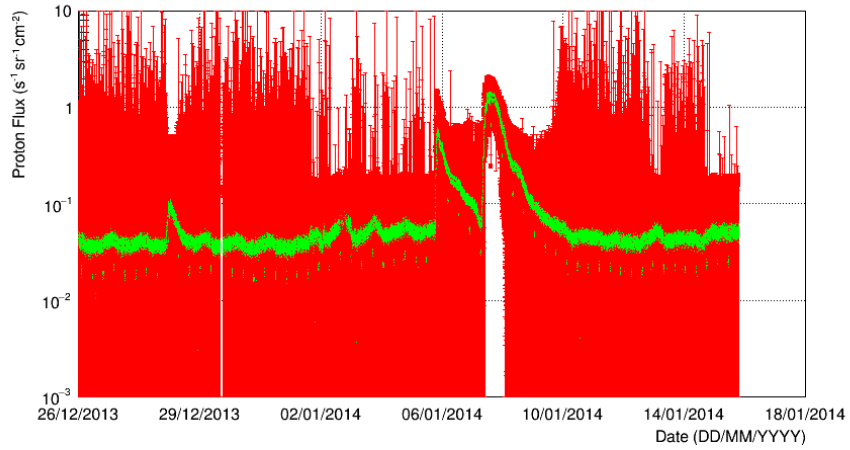


Figure 4.10: MFS proton flux spectra from 26/12/13 to 16/01/14, of energies between 94.87 MeV and 110.61 MeV.

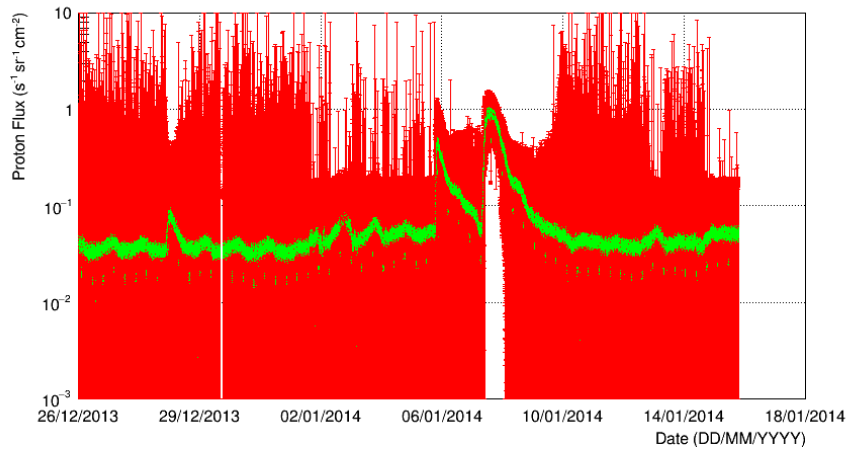


Figure 4.11: MFS proton flux spectra from 26/12/13 to 16/01/14, of energies between 110.61 MeV and 128.96 MeV.

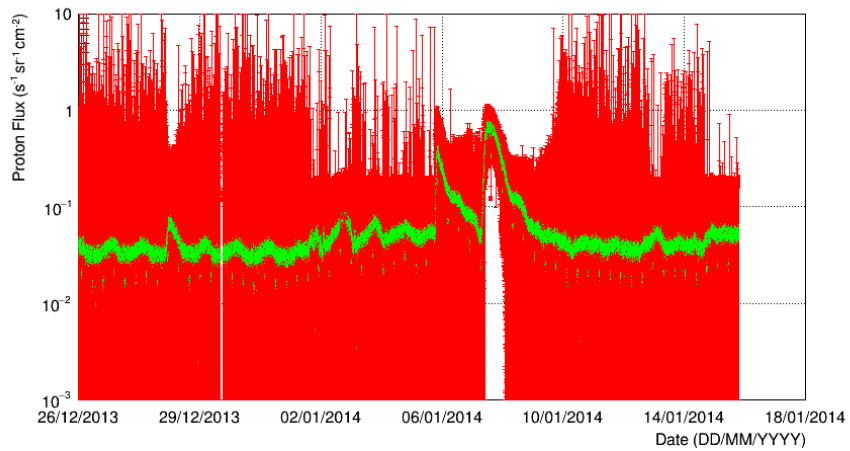


Figure 4.12: MFS proton flux spectra from 26/12/13 to 16/01/14, of energies between 128.96 MeV and 150.36 MeV.

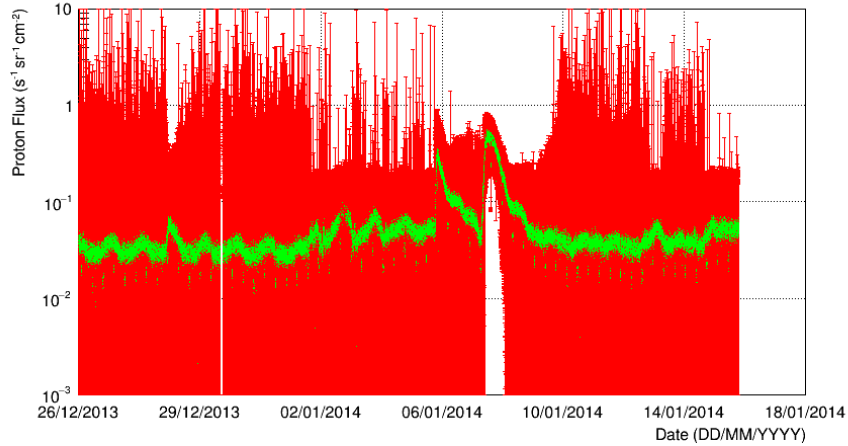


Figure 4.13: MFS proton flux spectra from 26/12/13 to 16/01/14, of energies between 150.36 MeV and 175.30 MeV.

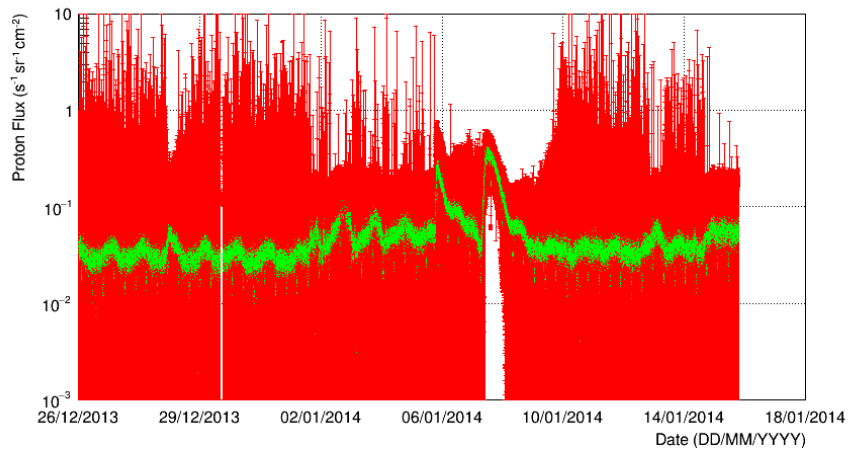


Figure 4.14: MFS proton flux spectra from 26/12/13 to 16/01/14, of energies between 175.30 MeV and 204.39 MeV.

around midday of 06/12/2014 and the largest peak starting about midnight of 08/12/2014. These are all caused by solar activity (SEPs) as they are clearly not part of the baseline, which is due to contributions from stable fluxes of GCRs and trapped particles on earth's magnetic field. Regarding the oscillations in the flux starting around 02/01/2014, before the second peak, these include electron contamination on proton channels. At GEO altitude (approximately 36 thousand kilometres above the surface) where MFS is orbiting, there are trapped protons but, mostly, electrons in Van Allen belts. The oscillations happen due to the day-night cycle, confirmed by the fact that the period of these oscillations is about 1 day. This is because the magnetosphere is asymmetric due to the electrically charged solar winds that deform the earth's magnetic field. As a result, the areas facing the sun are more densely populated by charged particles (yielding higher count-rates by MFS) than the areas away from the sun (conversely yielding relatively lower count-rates). These oscillations are more pronounced before the large peaks, which indicates that the belts were charged by a solar flare that preceded the coronal mass ejection responsible for the proton peaks. Considering the fact that it takes SEPs three to four days to travel from

the sun to earth [23], the 4 day delay between the day-night oscillations and the peaks seem to confirm this.

Proton flux fitting parameters

As discussed in chapter 3, proton flux spectra are assumed to have the shape of a power law with two unknown parameters, k and α as can be seen in equation 3.3. For each point in time, a fit to this power law yielded the best value that both parameters should take, explicit in figures 4.15 and 4.16.

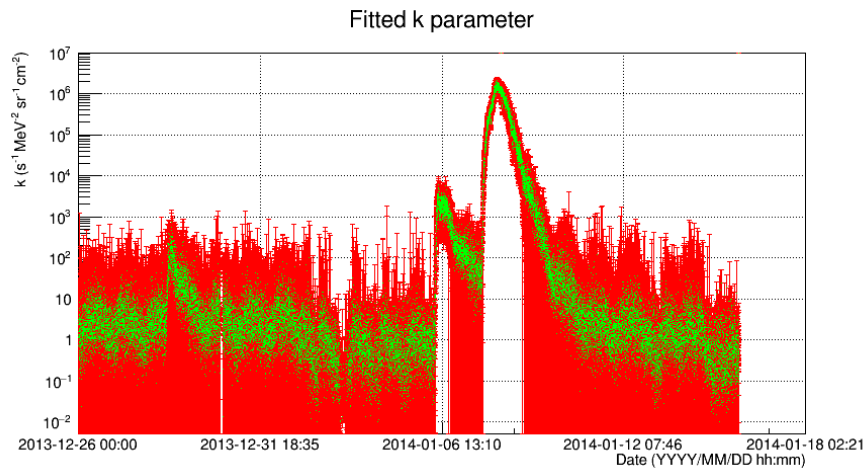


Figure 4.15: Proton flux k parameter.

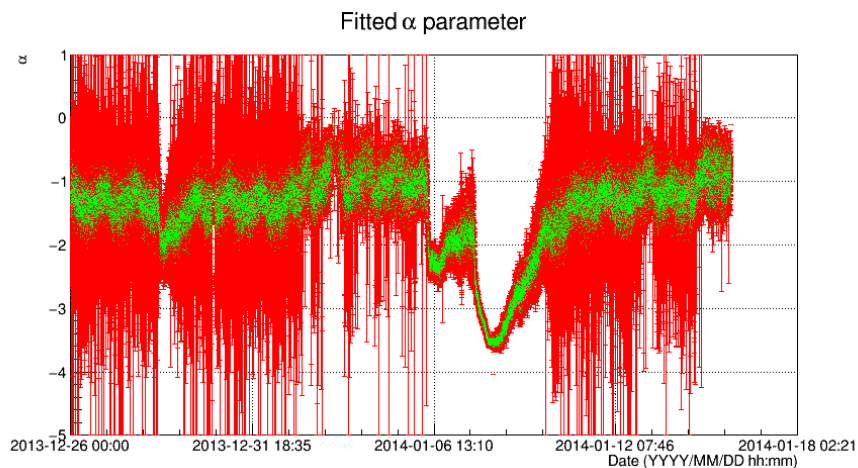


Figure 4.16: Proton flux α parameter.

The shape of the graph for k parameter should be, and it is, basically the same as the flux graphs because k is simply the value of the flux (as defined in equation 3.3) when $E = 1\text{MeV}$. The graph regarding α has an inverse dependence of k , which is what allows for reasonable results. k and α range from 10^{-1} to 10^6 and from around -4 to near zero, respectively. Large k values combined with the near zero α values would result in a near flat spectrum with large y-value at the origin, yielding very large fluxes, especially at high energies. Conversely, small k values coupled with large absolute values of α would yield rapidly declining spectra with very little area and consequently almost inexistent fluxes for

any energy.

This balance between both parameters that allows for reasonable results can be seen on figure 4.17. Here, a histogram with a number of bins twenty times smaller than the number of data points is plotted. This binning ensures that there is visible overlap of data, presented as a colour scheme, which indicates the relative density of points on the graph. For visual convenience, the width of the bins follow a base ten logarithmic scale on the y-axis so that all bins appear to be the same size on the graph.

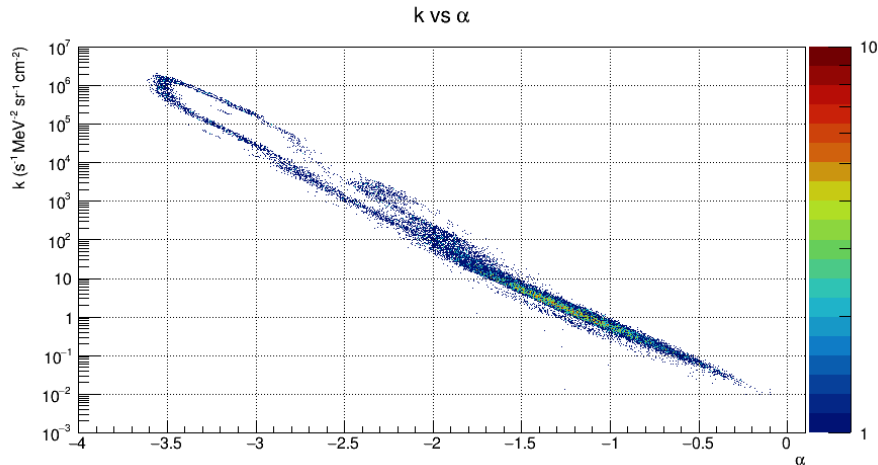


Figure 4.17: Proton flux k vs α parameter.

This exponential (mind that k on y-axis is presented in base ten log scale, so a straight line does not represent linear behaviour) relation between both parameters is satisfactorily clear, suggesting that the method used worked fairly well on this particular case.

Proton channels counts reconstruction

One convenient way of understanding how reliable the method is is to reproduce the detector's counts in the channels, from the determined flux spectra themselves. This is done simply by using equation 3.2 to retrieve each channel's counts with the obtained flux, for each time interval. Ideally the reconstructed data should perfectly match the actual data. In reality that does not happen, at least due to statistical uncertainties. By comparing both datasets however, we can check for any systematic biases or effects and evaluate the performance of the method's reconstruction procedure.

By inspecting these ten graphs it can be immediately seen that the reconstructed data does not fully match the measured one, but not by always over or underestimating it. Channels 1, 2 and 9 are overestimated, channels 3, 4, 5, 7, 8 and 10 are underestimated and channel 6 seems to be in a rather good agreement with the actual data.

The main factor likely to be responsible for these results is the fact that during the whole sample period channels 3, 4 and 5 registered more counts than channel 2 and even channel 1, before the latter was contaminated by the electron increased density due to the solar flare (see figure 4.1). This suggests that the behaviour of the flux for this time window does not entirely follow a power law, otherwise higher energy channels would consistently present fewer counts than the preceding one. By forcing

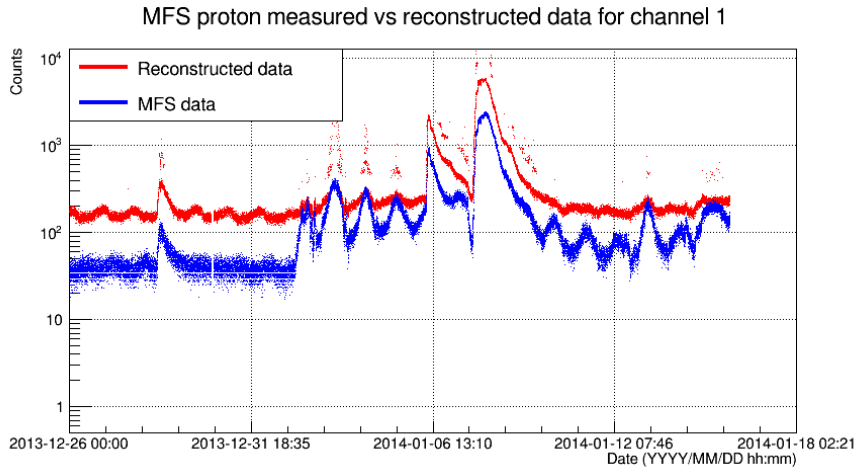


Figure 4.18: Proton reconstructed counts vs measured data from MFS

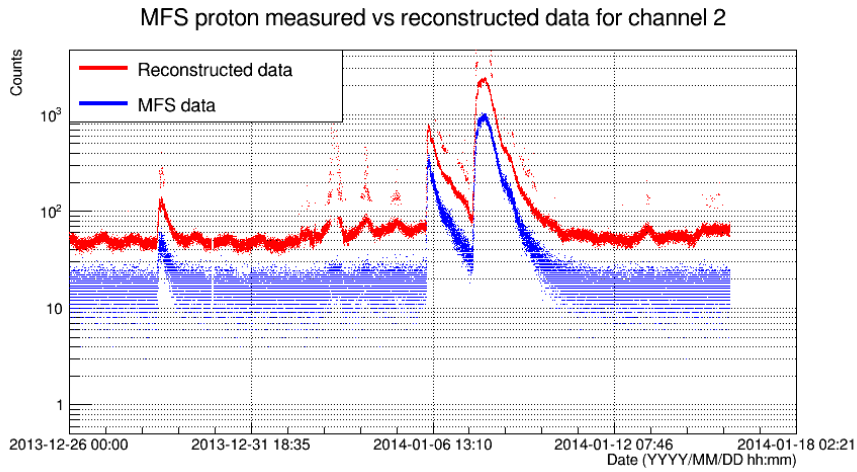


Figure 4.19: Proton reconstructed counts vs measured data from MFS

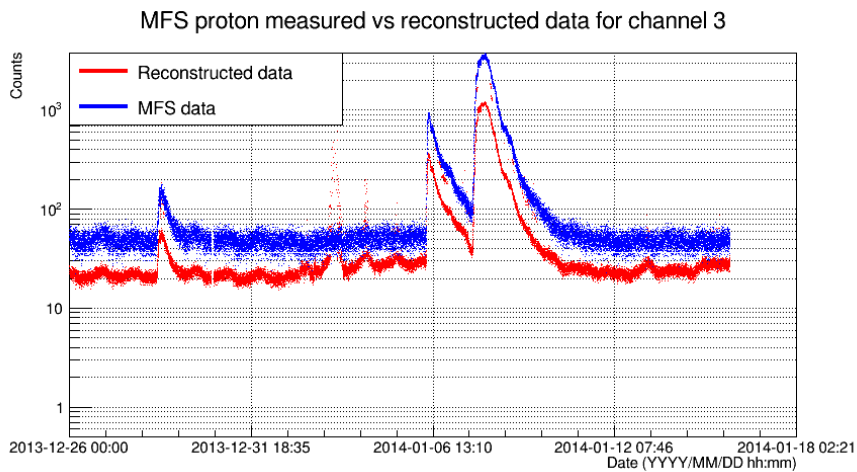


Figure 4.20: Proton reconstructed counts vs measured data from MFS

such a model onto the flux, reconstructed data will mandatorily be larger for lower channels, making it impossible for, say, channel 3 to have more counts than channel 1 (which consistently happens with measured data). This explains why channels 1 and 2 are overestimated, while channels 3 and beyond

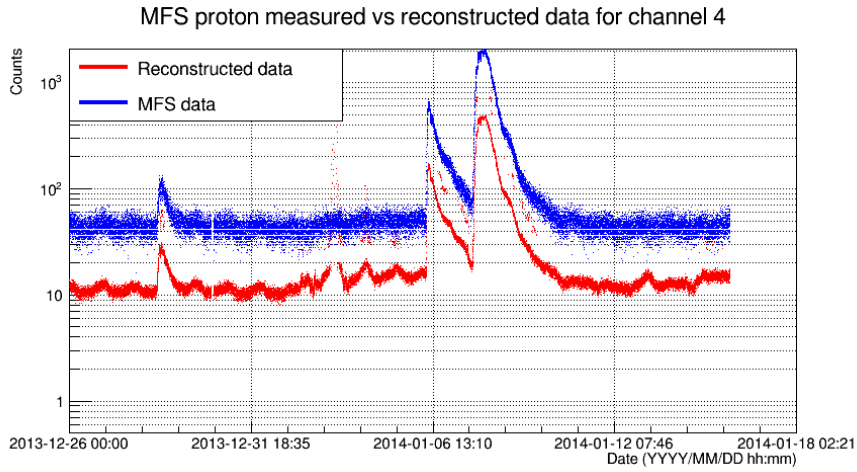


Figure 4.21: Proton reconstructed counts vs measured data from MFS

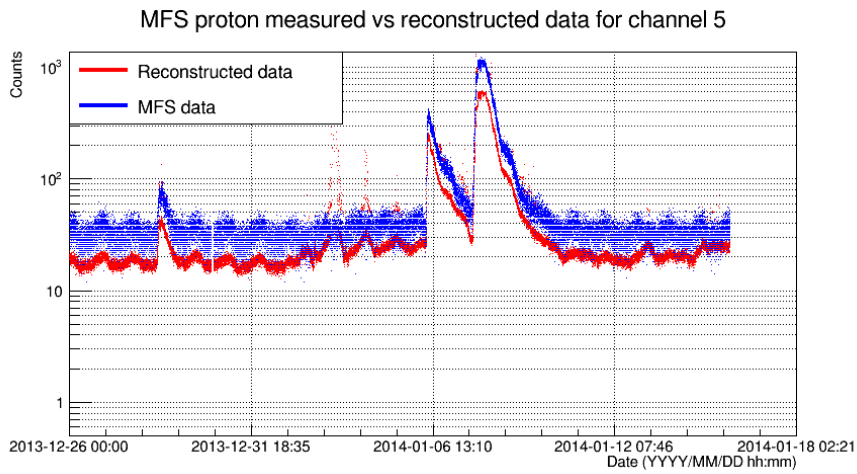


Figure 4.22: Proton reconstructed counts vs measured data from MFS

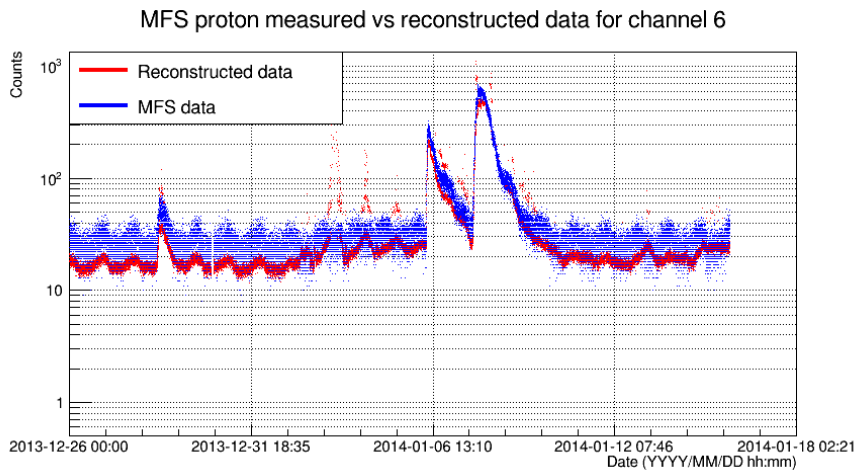


Figure 4.23: Proton reconstructed counts vs measured data from MFS

are generally underestimated.

Despite all this, MFS fluxes determined by this method seem to be reasonable when compared with flux spectra obtained with a different unfolding method, from another detector in a different GEO satellite

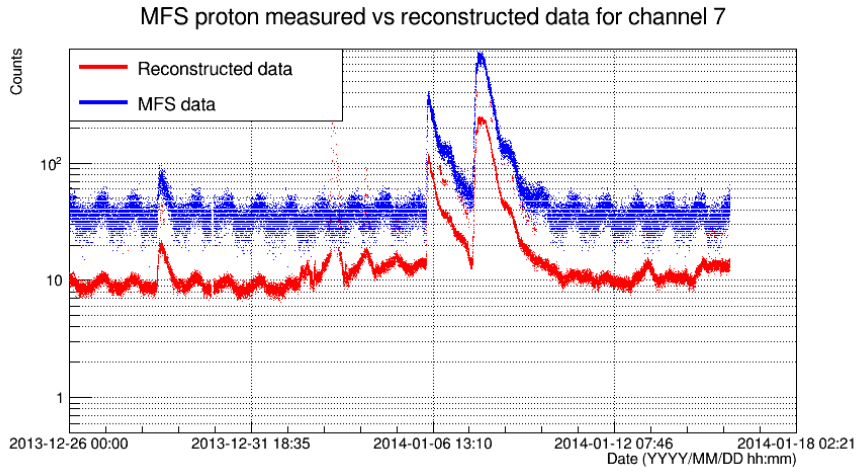


Figure 4.24: Proton reconstructed counts vs measured data from MFS

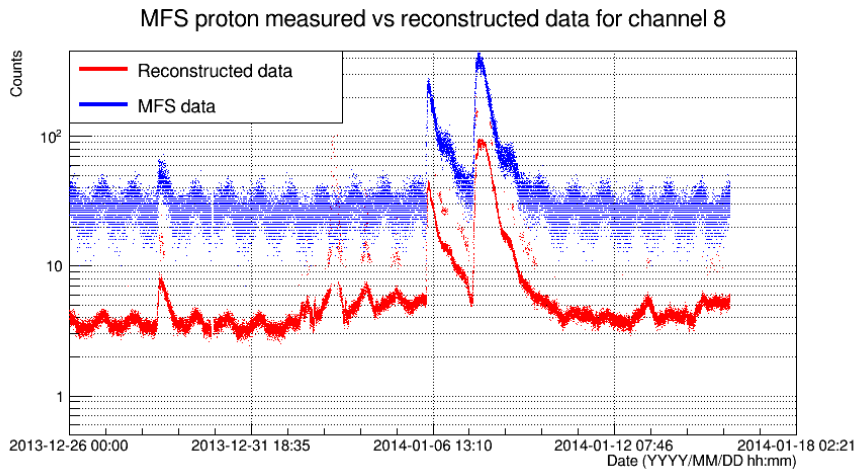


Figure 4.25: Proton reconstructed counts vs measured data from MFS

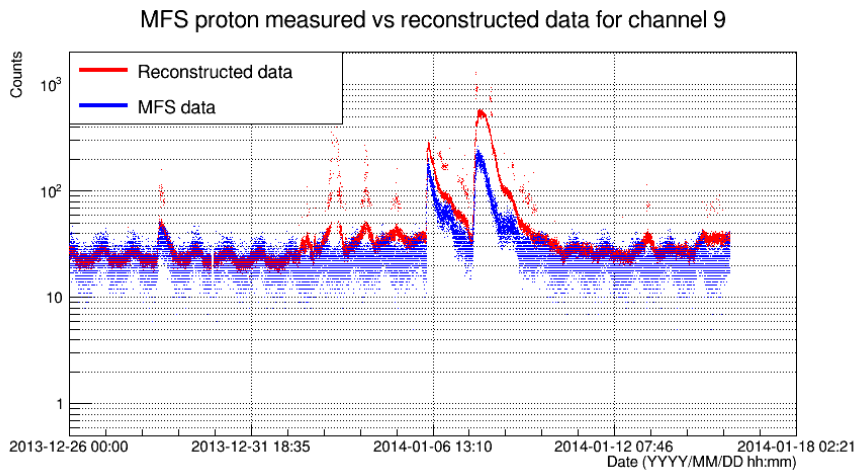


Figure 4.26: Proton reconstructed counts vs measured data from MFS

, as will be discussed in section 4.1.3.

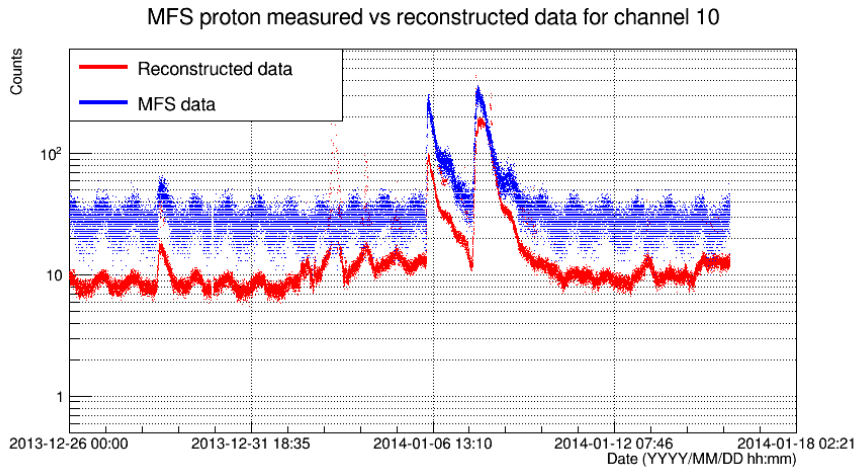


Figure 4.27: Proton reconstructed counts vs measured data from MFS

4.1.2 Electron flux spectra

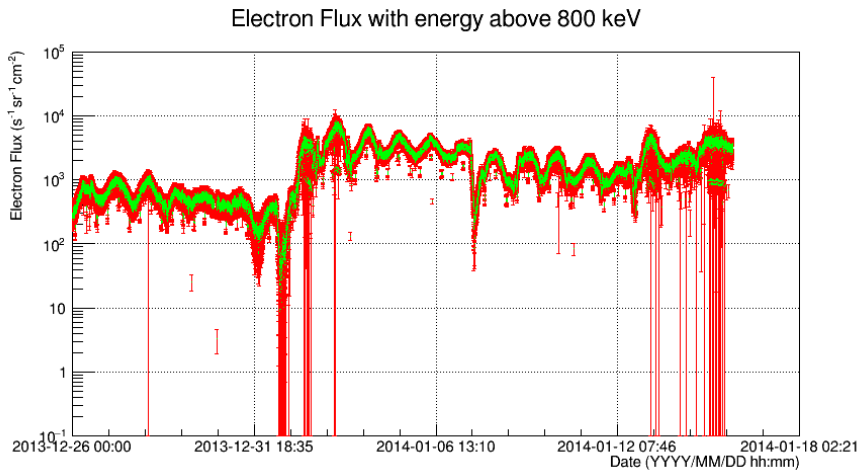


Figure 4.28: MFS electron flux from 26/12/13 to 16/01/14

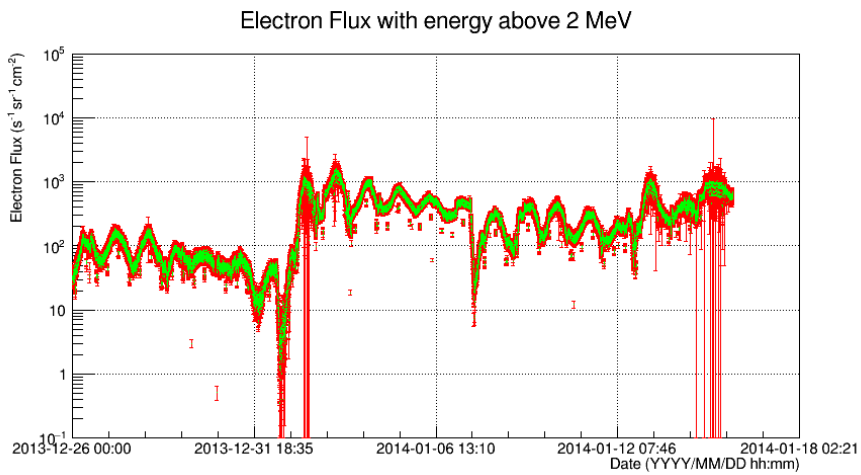


Figure 4.29: MFS electron flux from 26/12/13 to 16/01/14

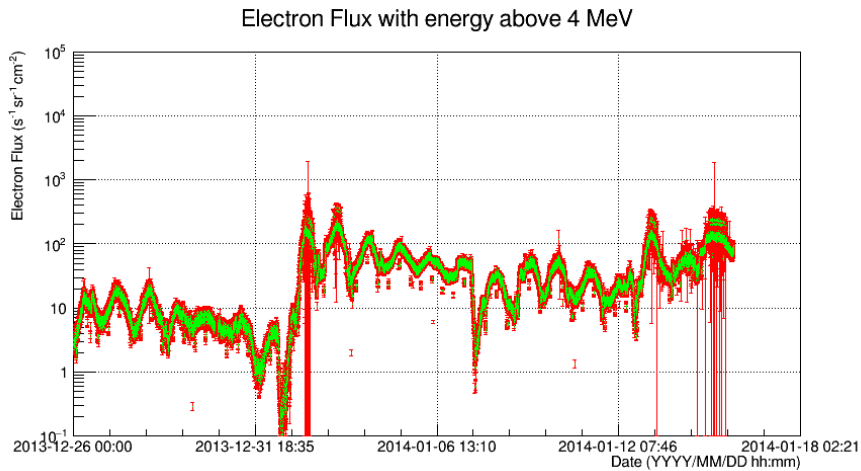


Figure 4.30: MFS electron flux from 26/12/13 to 16/01/14

The first thing that one might notice is that the shape of the flux spectrum does not change along energy intervals, even though different MFS channels registered different spectra (see figure 4.2, where it can be seen that channels 5, 6 and 7 are basically shapeless with barely any signal). This is due to the fact that the method used assumes a shape for the flux (a power law) so it finds the parameters that best predict the data points and then forces this law on the flux. Adding the fact that some channels contain much larger samples (specially channel 1), the overall shape of the flux along time is modelled after mainly these channels. Thus the only difference between spectra of different energy intervals is a scale factor.

The spectra can be divided into two zones: a pre and a post SEP onset zone. At about 02/01/14 a solar flare hits MFS, charging the belts and increasing the electron density, creating a long lasting bias that is present throughout the rest of the graph. Aside from that, the day-night oscillations are very clearly visible and seem to be stable around a fixed y-value, both pre and post flare. This implies that for this time period most electrons at GEO altitude are trapped on Van Allen belts having stable fluxes, without any unstable or eventful sources contributing to large peaks.

Electron flux fitting parameters

Like how it was stated with protons, the shape of the graph for k parameter is the same as the flux, since $k = \phi(E = 1MeV)$. Unlike proton results however, α does not show an inverse dependence to k . If there's a tendency at all, it is for both shapes to somewhat match. On figure 4.33 we can see that the plot of k vs α has an unformed shape with positive slope, confirming this. This means that higher values of the flux are determined by both a higher k and a lower absolute value of α that result in a more slowly declining high y-value at the origin spectrum. The opposite for lower values of flux. The reason why the flux results are not nonsensical is because, unlike protons, the value of the α parameter oscillates between -2 and -4, while k oscillates between 100 and 10000, preventing linear-like or very small y-value at the origin functions (respectively α and k near zero).

Regarding figure 4.33, just like with protons, a histogram with a number of bins twenty times smaller

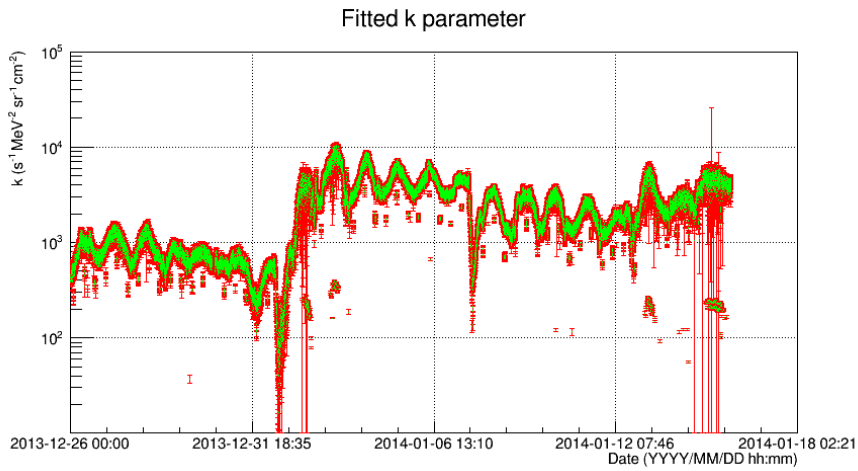


Figure 4.31: Electron flux k parameter

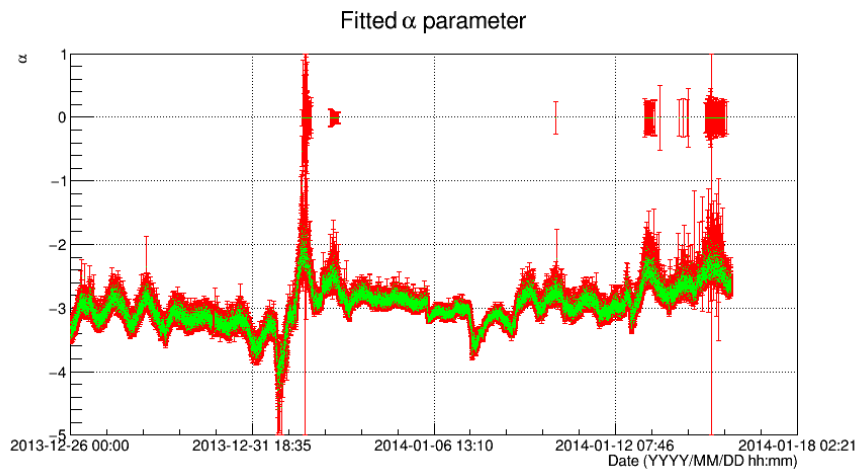


Figure 4.32: Electron flux α parameter

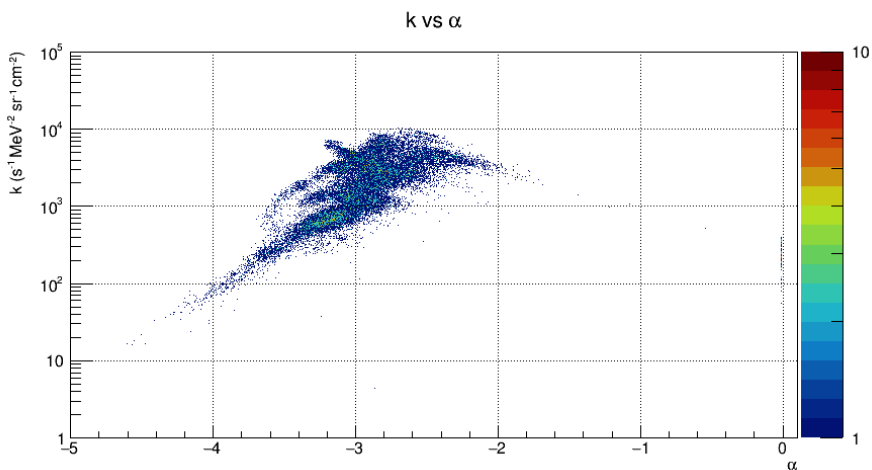


Figure 4.33: Electron flux k vs α parameter

than the number of data points is plotted, to allow for a visible overlap of data, presented as a colour scheme. The width of the bins also follow a base ten logarithmic scale on the y-axis. As can be seen, data is evenly spread, so the relation between both parameters does not seem to follow a well defined

trend beyond its overall shape.

Electron channels counts reconstruction

As with protons, data for all channels was reconstructed to get a sense of how reliable the method is for the analysis of incoming electrons.

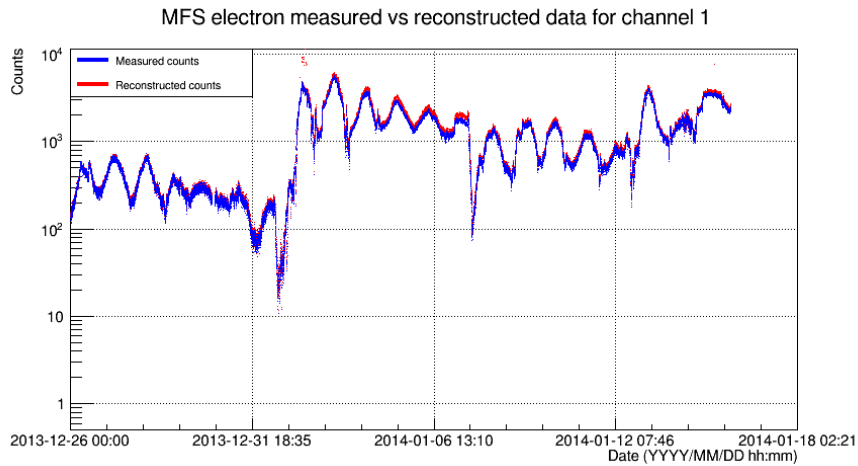


Figure 4.34: Electron reconstructed counts vs measured data from MFS

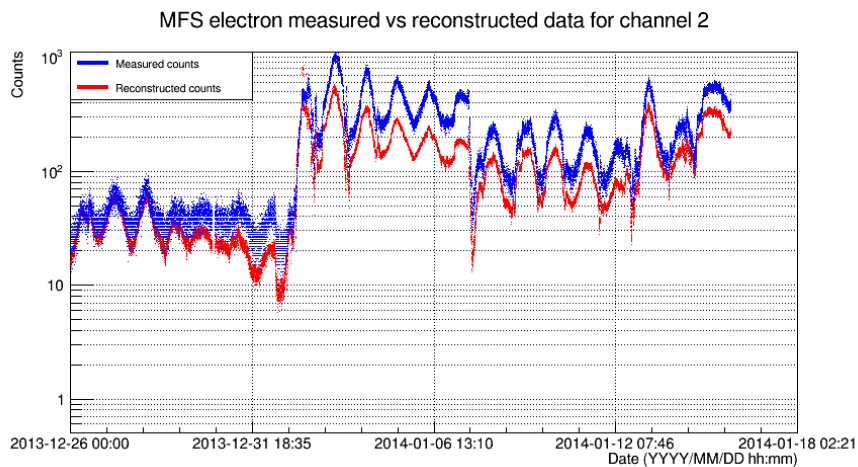


Figure 4.35: Electron reconstructed counts vs measured data from MFS

Reconstructed counts for electron channels show a very good match with channel 1 measurements (slightly overestimate) but underestimate channels 2 and 3. Channels 4 and 5 peak shapes are well reproduced and the remaining channels are shapeless due to the lack of signal, while reconstructed counts always keep a consistent shape as previously explained.

These results show that channel 1 high statistical weight is dominant in the shaping of the flux and the method faithfully reproduces its measurements. While the next two channels present well determined shapes they are underestimated as a compensation of the slight overestimate on channel 1 (one should keep in mind that channel 1 has much more statistics, so a "slight" overestimate can be quite large when compared to other channels). Channel 1 response function is much larger for any primary energy than

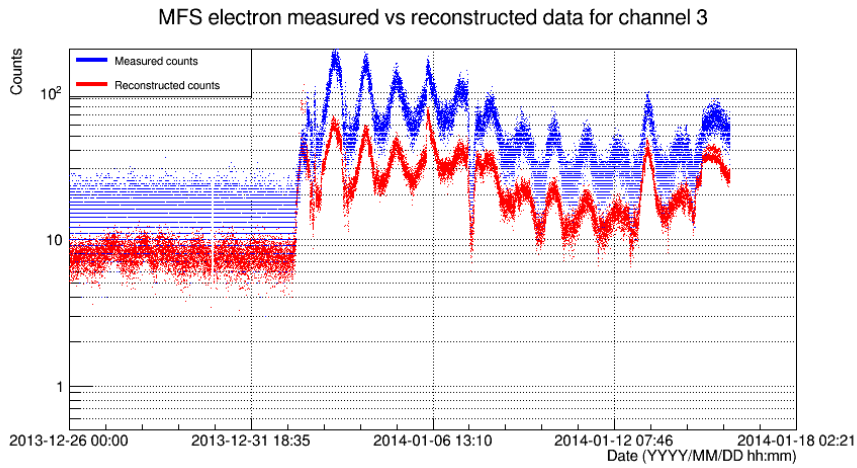


Figure 4.36: Electron reconstructed counts vs measured data from MFS

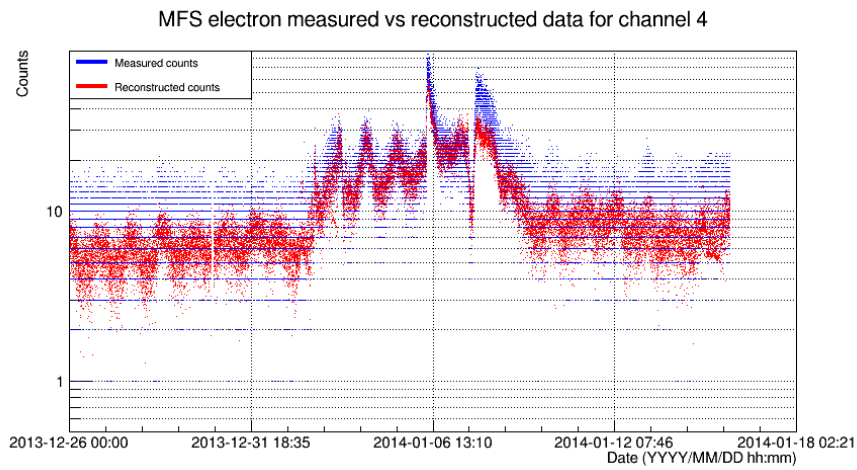


Figure 4.37: Electron reconstructed counts vs measured data from MFS

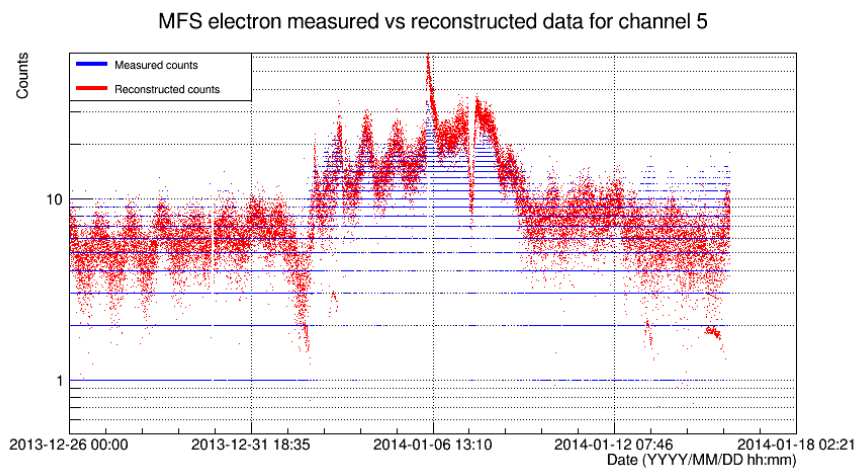


Figure 4.38: Electron reconstructed counts vs measured data from MFS

the others so it is no surprise that the former is so dominant.

This presents as a limitation to this method since it fails to reproduce the lack of signal on the last channels. As a side note, this method works best in theory on large sample sizes and many data

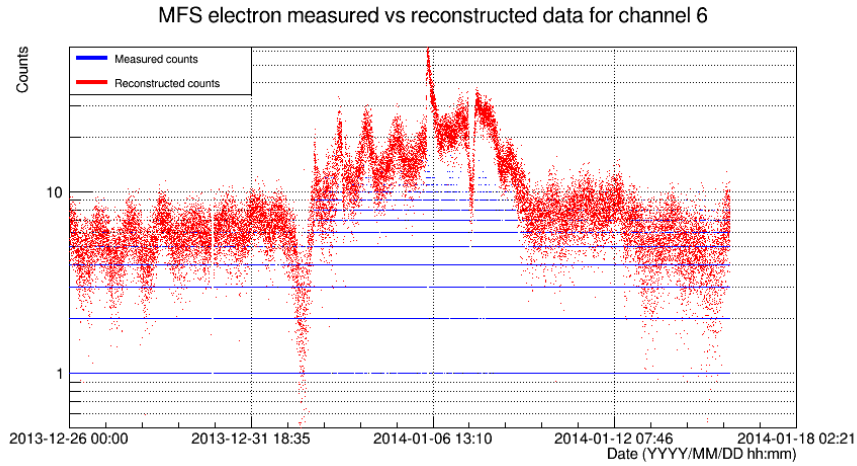


Figure 4.39: Electron reconstructed counts vs measured data from MFS

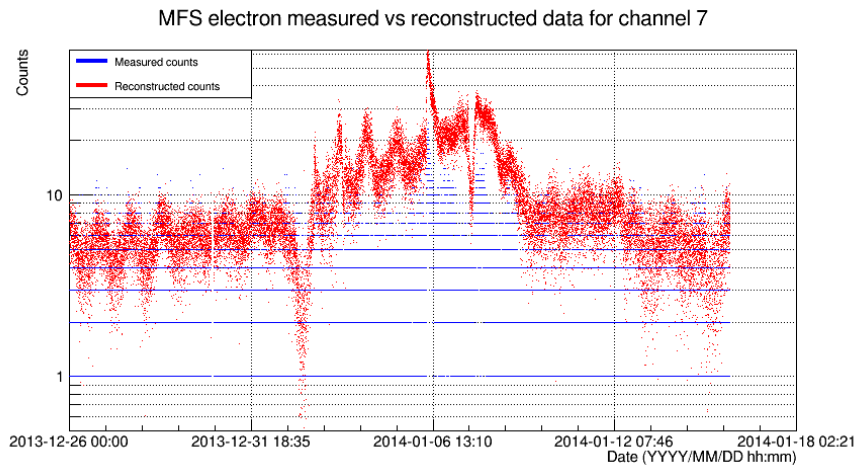


Figure 4.40: Electron reconstructed counts vs measured data from MFS

samples (channels). Fitting data with two fitting parameters and only three to four statistically relevant data points is likely to yield underwhelming results.

4.1.3 MFS vs. GOES flux spectra

To further validate the results obtained by MFS and the particular unfolding method used in this work a comparison with analogous results from a different experiment will be presented in this section.

This experiment is a part of the multimission *Geostationary Operational Environmental Satellite* (GOES) programme conducted under the North American *National Oceanic and Atmospheric Administration* (NOAA). Briefly, this is a programme that aims at collecting environmental data to support weather forecasting and monitoring and meteorological research [24]. Amongst this, charged particles detectors are also built in the satellites, named EPEADs (Energetic Proton Electron Alpha Particle Detector), providing data on proton and electron fluxes. Specifically, in this work MFS results are compared with results from GOES-15, launched on March 4th 2010. It was the latest launched weather satellite of this project operating during the studied time interval, which was from December of 2013 to January of 2014.

MFS vs. GOES proton flux spectra

GOES provides differential proton flux (as described by equation 3.3) spectra for six different energies, which were replicated with the maximum likelihood estimate method for comparison and are shown below.

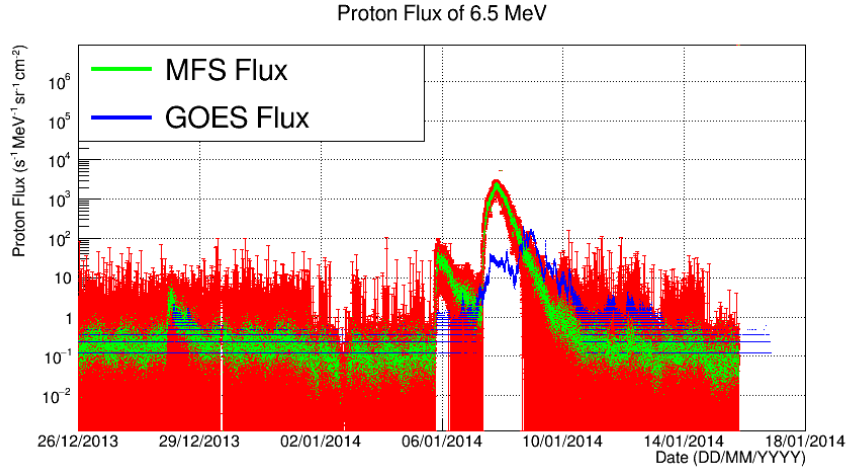


Figure 4.41: MFS vs GOES proton flux spectra, from 26/12/13 to 16/01/14.

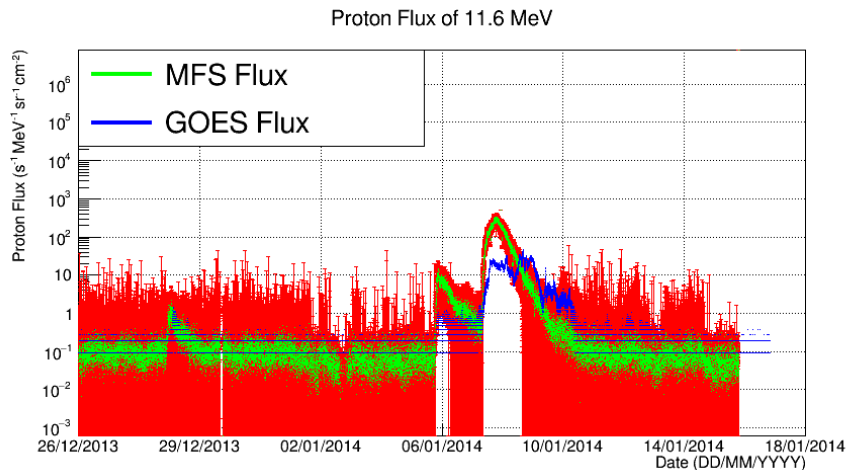


Figure 4.42: MFS vs GOES proton flux spectra, from 26/12/13 to 16/01/14.

The three peaks that were previously discussed on section 4.1.1 were also detected by GOES and show a good match timewise. Regarding intensity, MFS and GOES are in best agreement on medium-range energies, as they are fairly close to each other for fluxes of 30.6 MeV, 63.1 MeV and 165 MeV.

A reason as to why at lower energies both graphs are not in such agreement could be due to the fact that the maximum likelihood estimate method used assumes a power law that forces lower energy fluxes to be obligatorily superior to relatively higher energy fluxes ($\phi(E_1) > \phi(E_2), E_1 < E_2$). As already showed (figure 4.1), lower energy channels happened to register fewer counts than medium energy channels. Thus ideally an unfolding method would yield lower fluxes for lower energies and higher fluxes for medium energies. This is not the case for GOES either however, because the third and tallest peak reduces as energy increases. This is not conclusive since we are looking at energy points largely

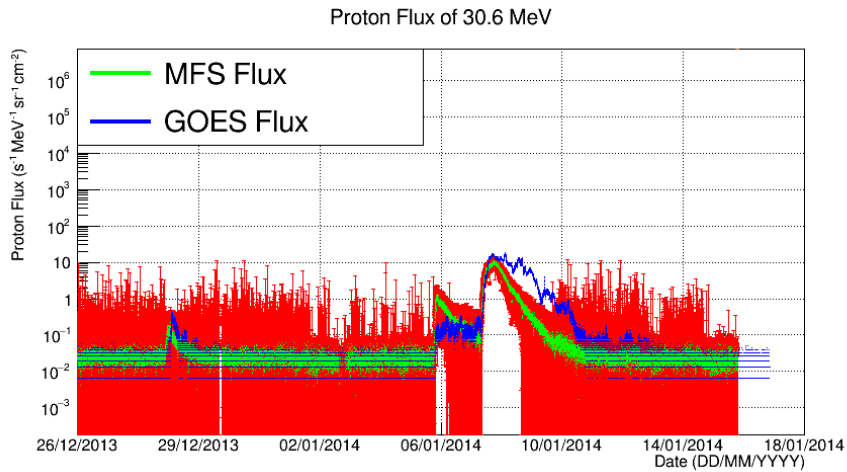


Figure 4.43: MFS vs GOES proton flux spectra, from 26/12/13 to 16/01/14.

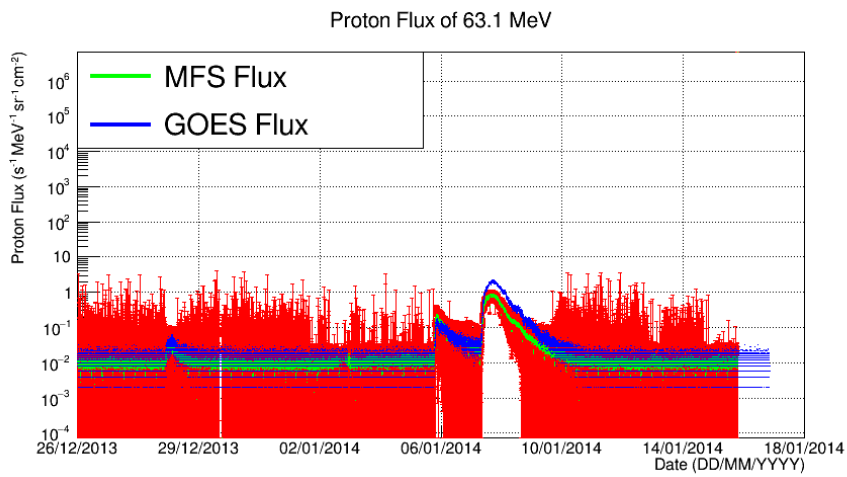


Figure 4.44: MFS vs GOES proton flux spectra, from 26/12/13 to 16/01/14.

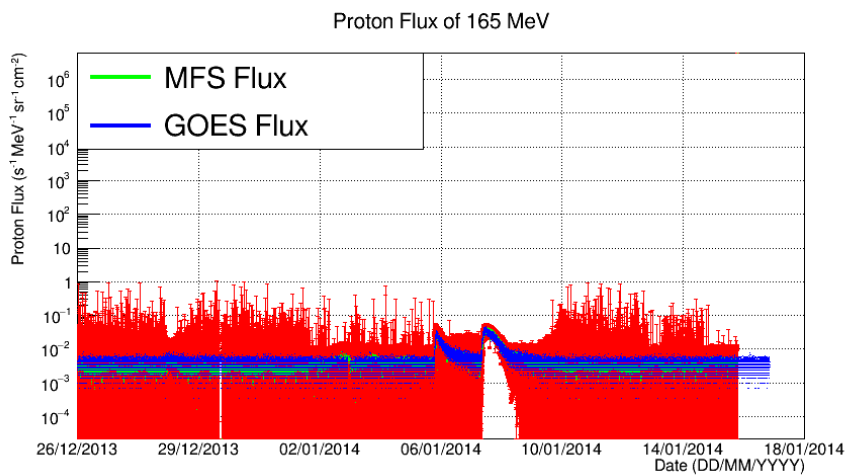


Figure 4.45: MFS vs GOES proton flux spectra, from 26/12/13 to 16/01/14.

spaced between each other. The only way to confirm if GOES indeed registers a downward trend on the flux over energy would be to look at fluxes of energies between 11.6 MeV and 30.6 MeV and check if they do not increase at some point.

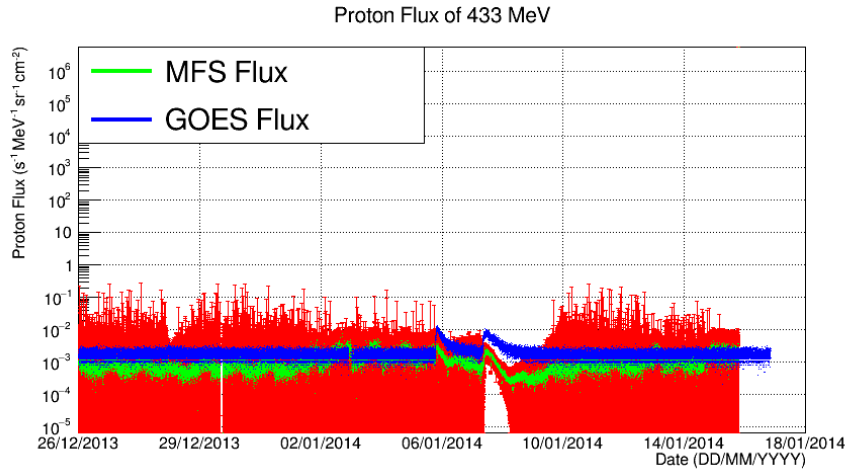


Figure 4.46: MFS vs GOES proton flux spectra, from 26/12/13 to 16/01/14.

GOES spectra also looks flatter on the baseline hinting that maybe MFS proton channels are more easily contaminated by the trapped electrons, creating the characteristic one day period wave-like shape of the baseline. On the other hand, the more discrete-like (with relation to the y-axis) shape of GOES fluxes, particularly on the baseline zones, suggests that it works with less statistical data than MFS, because this shape is likely caused by the data consisting on small integers.

Regarding the last graph of the 433 MeV flux, MFS flux loses its shape while GOES still presents two peaks. This would be because for very high energies the power law is reaching its asymptote near zero, breaking down the shapes that the flux time-spectra might have. Also this very high energy case was neither simulated and present under the response functions nor were MFS energy channels supposed to measure such energies, so one should never expect the best results for this case.

Nevertheless, generally speaking MFS and GOES seem to agree satisfactorily with one another for the SEP periods, reinforcing the idea that the method developed in this work works reasonably well with protons.

MFS vs. GOES electron flux spectra

Regarding electron fluxes, GOES fluxes are presented in an integrated form. Obviously MFS fluxes were determined the same way for them to be comparable, so the units expressed on the graphs are in $s^{-1} cm^{-2} sr^{-1}$. For energies greater than 800 keV the baseline area seems to be in somewhat agreement with GOES, however not so much in the post flare area, by a bias of an order of magnitude. The shape of MFS flux agrees with GOES however, except it seems to be in phase opposition. This is because GOES is in GEO orbit opposing MFS, since MFS is located at $24.8^{\circ}E$ in longitude, while GOES-15 is at $135^{\circ}W$ ($225^{\circ}E$), separated by a longitude interval of 200° [7]. This means that the day-night cycle is inverted, thus yielding these opposing oscillations.

The MFS flux with energy above 2 MeV seems to be in fair accordance with GOES for the post flare area. Here two things should be noticed about GOES results.

Firstly, on the pre flare area there are no more oscillations, meaning that no electrons with more than

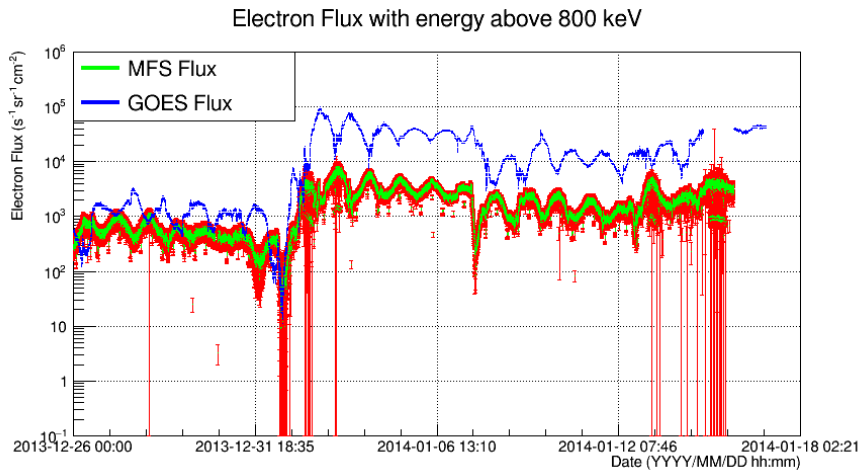


Figure 4.47: MFS vs GOES electron flux spectra, from 26/12/13 to 16/01/14.

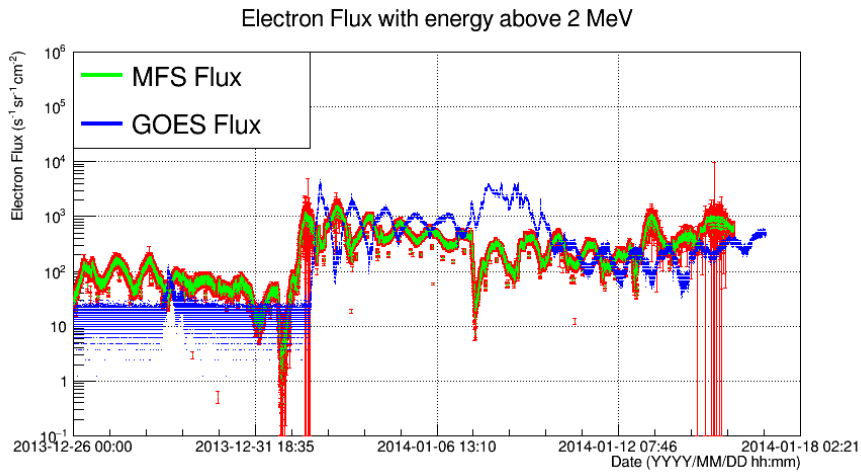


Figure 4.48: MFS vs GOES electron flux spectra, from 26/12/13 to 16/01/14.

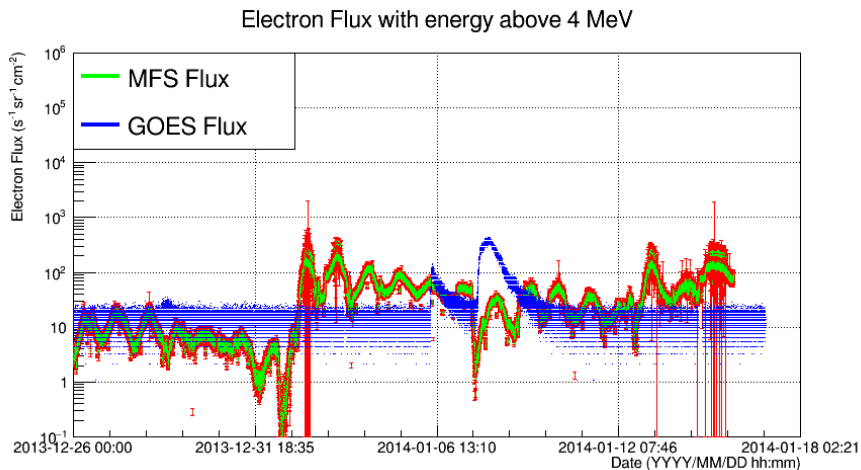


Figure 4.49: MFS vs GOES electron flux spectra, from 26/12/13 to 16/01/14.

2 MeV should be detected. This is confirmed by MFS electron data in figure 4.2 where we can see that channels 3 and beyond (that only detect electrons with energies higher than 2-3 MeV) only oscillate after the flare hit the satellite; before that they register residual signal.

Secondly, GOES electron results seem to be quite influenced by protons. The first proton peak is clearly visible on the pre flare area. And the second and third proton peaks also increase the electron flux as can be seen by the unformed bulge on an otherwise well defined wave-like flux.

MFS seems to have better results regarding proton contamination on electron channels as no proton peaks seem to have influenced the electron data. Regarding the oscillatory nature of the pre flare higher than 2 MeV flux: it is once again the result of the unfolding method forcing a shape, determined mostly by the high statistics of the first two channels, on the flux.

This becomes obvious for the flux with energies larger than 4 MeV, where GOES has virtually no electron signal (only nicely well defined proton contaminations) and MFS seems to have a lot going on. In reality, MFS higher energy electron channels barely have any signal as well, so the results would probably be very similar with GOES, minus the significant contamination, if the unfolding method did not assume a shape for the flux. So as it is, this last graph does not allow for any sort of fair comparison and no conclusion can be drawn from it.

4.2 "Baseline" analysed from April 18th to April 21st 2014

The maximum likelihood estimate method developed was also applied to the analysis of an uneventful time period. As can be seen by figures 4.50 and 4.51, there was barely any proton activity recorded in this time period, with the exception of the small peak registered by channel 2. This makes this time period useful for the analysis of electron fluxes when low solar activity is registered. The advantages of this is that residual proton signals will not contaminate as significantly the electron channels as in the case of a SEP. Also, in this period there is no solar flare affecting the Van Allen belts, so the signals obtained from MFS electron channels should reflect only the electron baseline in GEO.

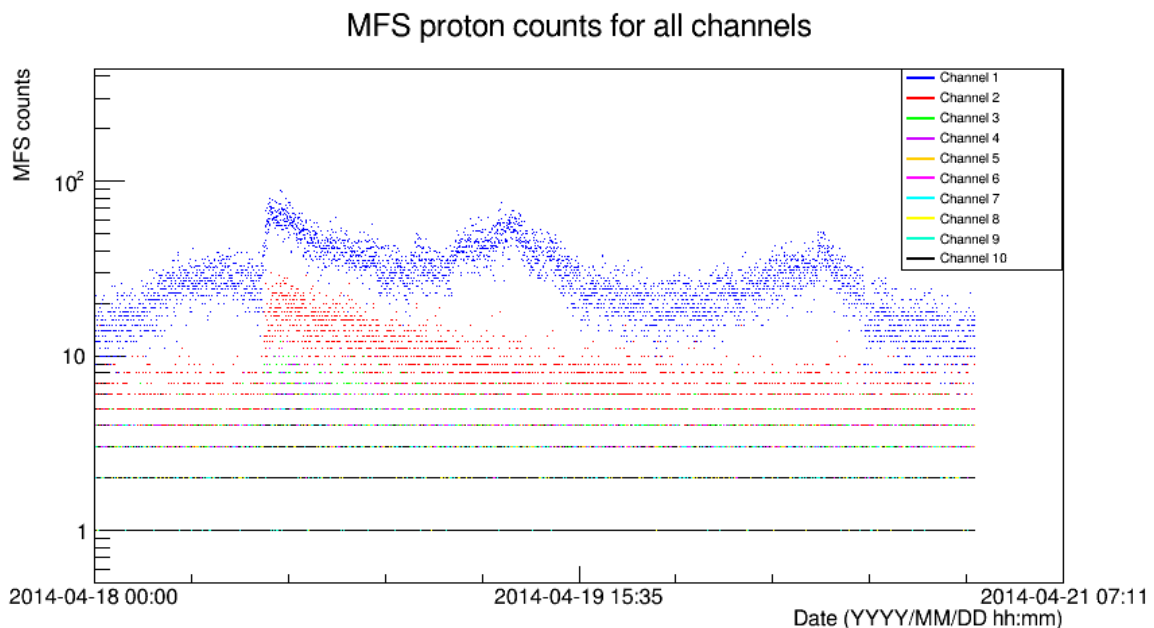


Figure 4.50: Data acquired by each MFS proton channel, starting at 18/04/2014 and ending at 21/04/2014.

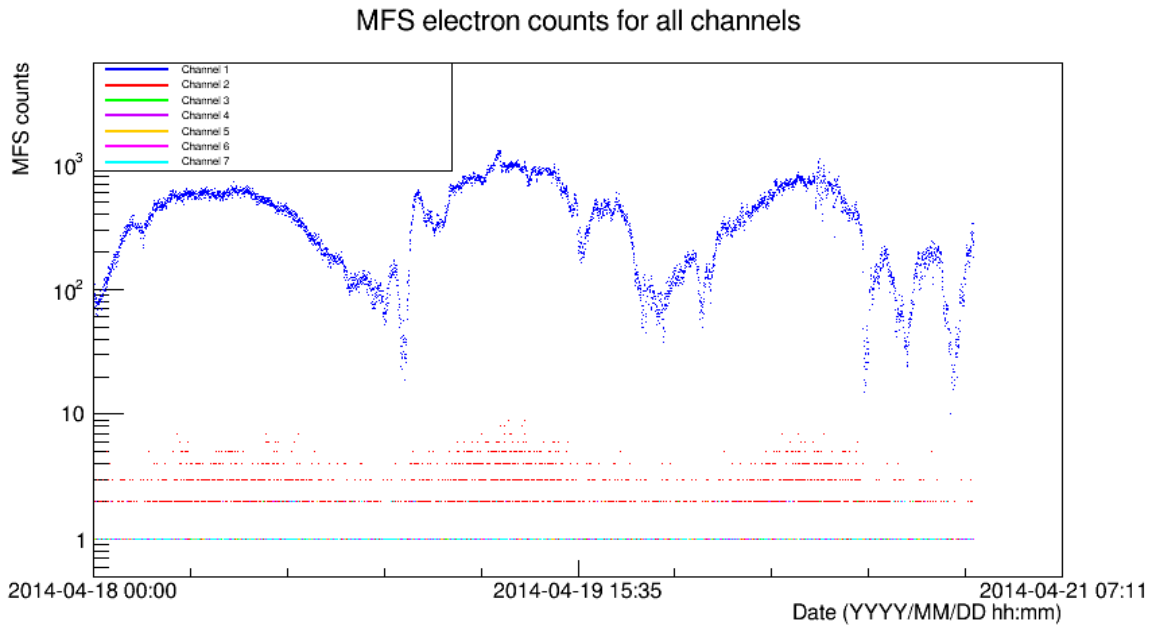


Figure 4.51: Data acquired by each MFS electron channel, starting at 18/04/2014 and ending at 21/04/2014.

Only electrons were analysed for this time period because they are the dominant contributor in GEO in the absence of SEP particles.

4.2.1 MFS electron flux spectra results and comparison with GOES

Figures 4.52, 4.53 and 4.54 show the fluxes obtained with MFS maximum likelihood estimate method compared with GOES fluxes.

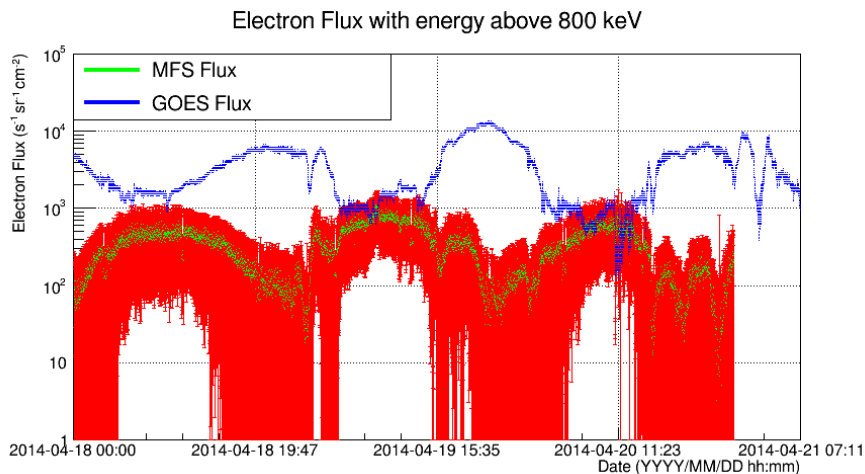


Figure 4.52: MFS vs GOES electron flux spectra, from 18/04/14 to 21/04/14.

Once again the phase opposition of the oscillations of GOES and MFS results, which were already explained, can be seen. Aside from that, both graphs shapes seem to reasonably match. But the most important characteristic to look for here is the level of the baseline and how it compares between the two satellites. Looking at figure 4.52 it can again be seen that GOES fluxes larger than 800 keV are one

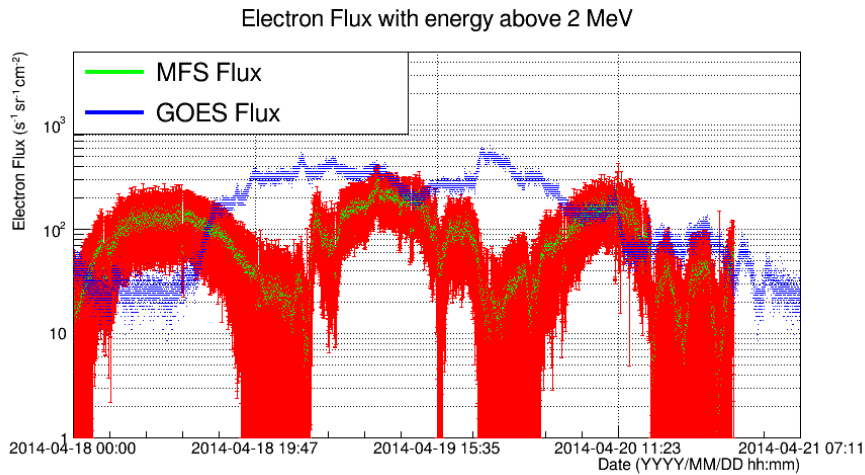


Figure 4.53: MFS vs GOES electron flux spectra, from 18/04/14 to 21/04/14.

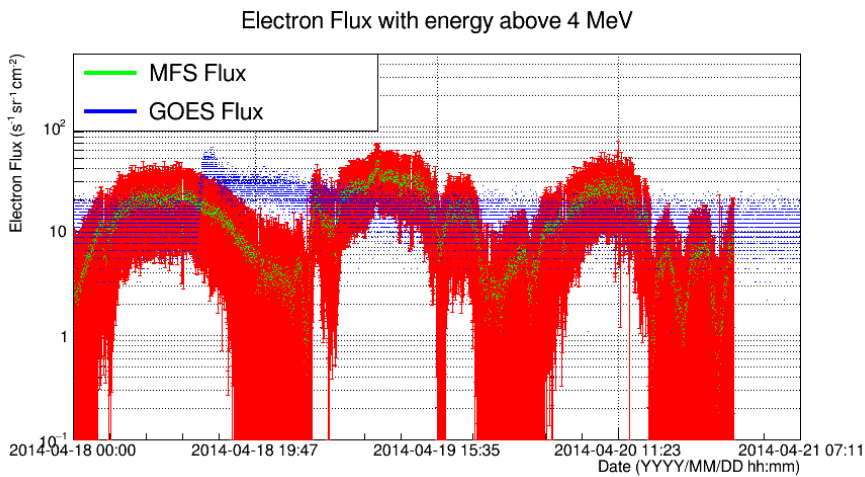


Figure 4.54: MFS vs GOES electron flux spectra, from 18/04/14 to 21/04/14.

order of magnitude larger than MFS, which is somewhat consistent with what was seen in the previous case analysed, although in figure 4.47 this was more evident post solar flare and during the whole SEP.

Looking now at the flux above 2 MeV, the shape of both graphs do not match each other anymore, like they did for the flux larger than 800 keV (once day/night cycle is factored in). This is again due to the forcing of a shape on the flux by the method developed in this work. Only channel 1 has relevant data and so it is forced upon all energies. However, the order of magnitude between both experiments is more similar, which had also happened during the SEP event (see figure 4.48). This reinforces the idea that the differences regarding the order of magnitude of the results is due to differences in the detectors themselves (their efficiency at particle detection, their susceptibility to other particle's contaminations, their level of electronic noise...) and not in the methods used to unfold the data.

As seen in the previous section, GOES electron data for higher energy fluxes, above 4 MeV, is practically non-existent. The same happens with MFS, although the maximum likelihood method fails to reproduce the lack of data for higher energy fluxes. It is a positive however that, differences in shape aside (which were already covered), both graphs are of similar magnitude. This means that both satellites and methods of data analysis yield similar baseline results when both have little data to work

with.

Another corollary of having to deal with low amounts of data is that the statistical uncertainty is relatively larger, ensuing less reliable results. Despite that, the method worked remarkably well with a 100% success rate of convergence, i.e. there were no data points that failed to produce a pair of parameters (during the SEP period analysed some data points would inevitably have to be discarded due to the method's failure in converging).

Electron flux fitting parameters

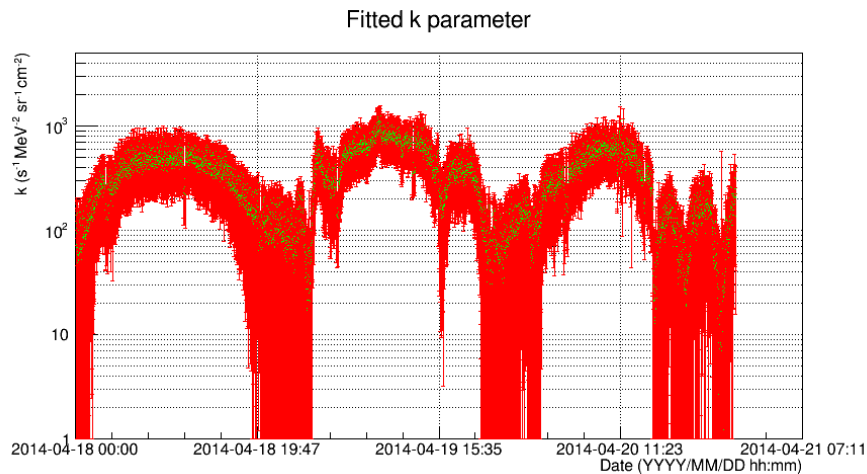


Figure 4.55: Electron flux k parameter

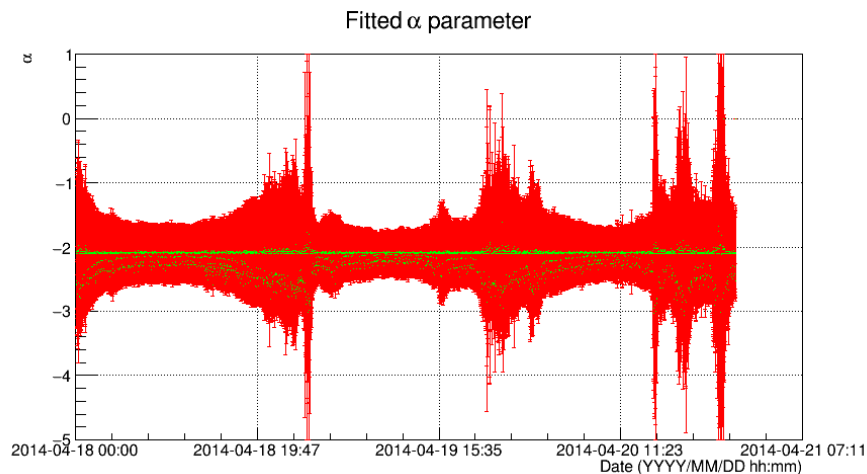


Figure 4.56: Electron flux α parameter

In this case the only interesting parameter is the α parameter, since k adopts the shape of the flux. As can be seen α is mostly constant (with a value of $\alpha \approx -2$), with slight oscillations, which is quite good because it reveals a consistent inverse-square law dependence on energy by the flux during baseline periods. When both parameters are plotted versus each other there's no visible tendency besides a saturated α with a value around -2 for several k parameters. The values of α further from -2 are a minority and probably instances where the method had more difficulties converging. Here, like in the

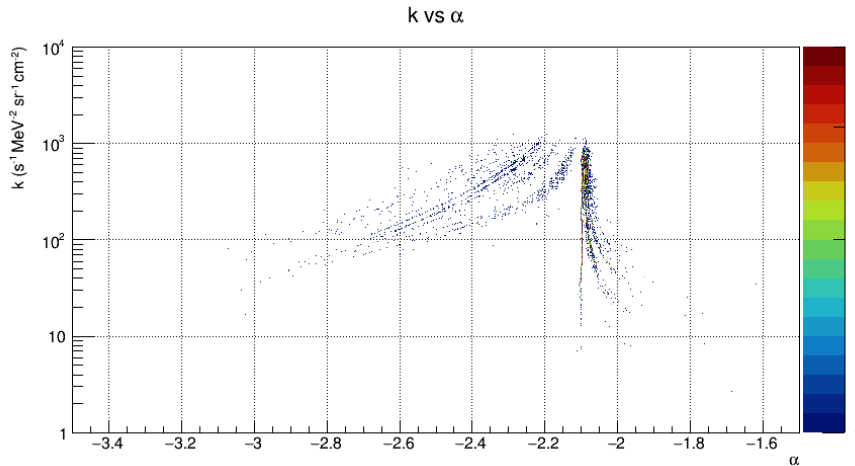


Figure 4.57: Electron flux k vs α parameter

previous cases, figure 4.57 is a histogram which indicates the relative density of points on the graph. Because there were less data points analysed (it is only a three day sample), the number of bins in the histogram is only one fourth of these.

Electron data reconstruction

Data for all channels was once again reconstructed to get a sense of how reliable the method is.

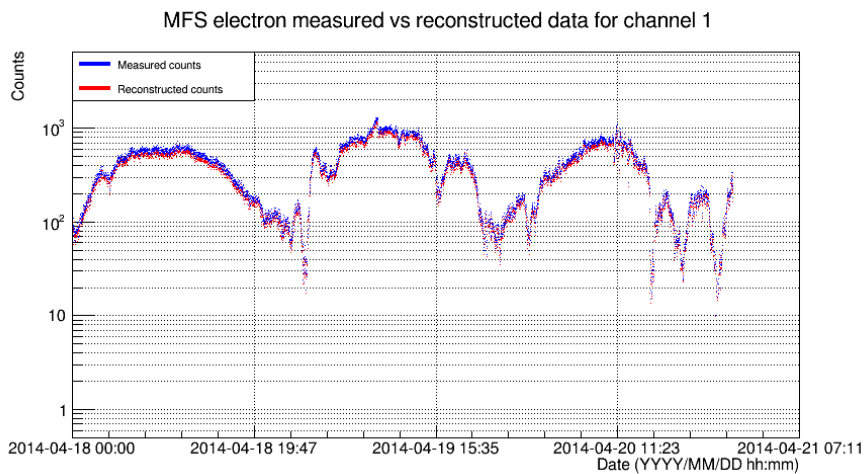


Figure 4.58: Electron reconstructed data vs measured data from MFS

Graphs for channels 4 to 7 are not shown because they are very much alike channel 3, seen in figure 4.60, where there's either one single count or none at all. As explained the reconstructed data will always have the shape that it has present on all figures shown because of the power law assumption used in the method. But as expected, data from channel 1 is very well reconstructed since this is the only channel with any relevant signal. The other channels are not faithfully duplicated at all since lack of signal is, as discussed, unreproducible by this method.

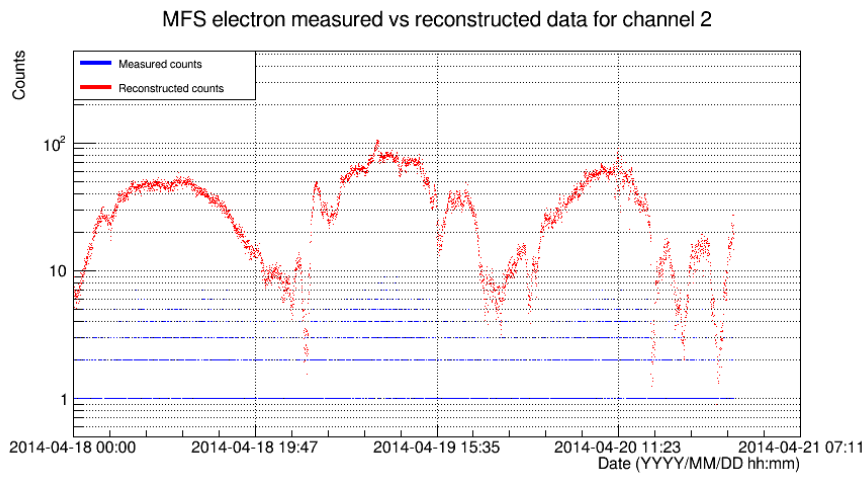


Figure 4.59: Electron reconstructed data vs measured data from MFS

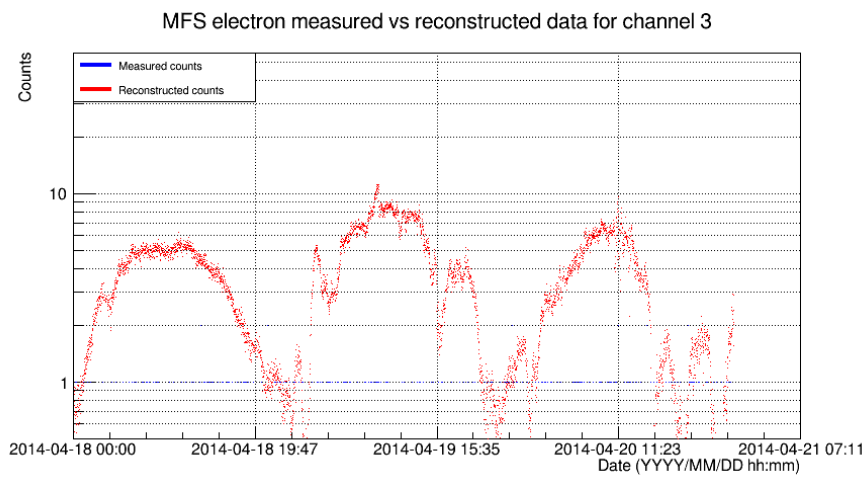


Figure 4.60: Electron reconstructed data vs measured data from MFS

Chapter 5

Conclusions

This work allowed the analysis of MFS data to be performed by the LIP team and was included in a paper published on IEEE TNS Journal [7]. So far researchers had to rely on particle fluxes provided by particle energy spectra reconstruction algorithms derived by external working groups. One advantage of this work was to perform the flux spectra generation through MFS raw data within LIP, so researchers know how it works, its limitations and characteristics. These will be discussed in this section, as well as further improvements or changes that could be done to the method developed in the future.

As stated, the method adopted in this work was the standard maximum likelihood estimate method to fit the data with a power-law. One major disadvantage of this method is the assumption of a fixed mathematical function that describes the spectral behaviour. The consequence of this assumption is the forced shape on the flux spectra, as described before in chapter 4. This is more problematic the greater the difference between the signal shapes present in different channels.

Another limitation of this type of method is that it needs large samples to work best, which sometimes was not the case, especially in the electrons case, for the higher energy channels. Higher energy channels had very residual response functions and barely any signal, which made the fitting process less viable by its own nature, since fitting three or four relevant data points to a function with two unknown parameters will not be ideal. In order to make this kind of method work better, MFS would need more energy channels with statistically relevant information on each of them. The fitting of proton data yielded better and more accurate results for this reason.

The method used in this thesis is a first order approach to the issue of obtaining flux spectra from MFS data, so it is simpler when compared to other methods used on the process of determining particle fluxes from registered counts by a telescope, such as the SVD and artificial neural networks, which means that it's less robust and universal. A method that does not assume a mathematical function *a priori* for the spectral shape might adapt better to any situation when a predefined function will not be the best to describe the data in all channels. Different methods that do not involve a fitting process may also yield better results when dealing with small samples of data. The simplicity of this method however, made changes and improvements easier and faster to implement; it is also good enough to validate simulations or data obtained from other GEO telescopes, since it yields results consistent with

GOES-15.

It should be noted that a rigorous comparison of results obtained from MFS and GOES-15 is not straightforward, because these detectors do not have the same build and detection characteristics. These are some of the issues regarding the inter-calibration of instruments sent to Space, making comparisons difficult. For the purposes of analysing the method implemented, consistent results when compared with GOES-15 is more important than a very good agreement on fluxes of specific energies. For instance, MFS low energy (800 keV - 2 MeV) electron flux results for the SEP event and the "baseline" time period were consistently lower than GOES by an order of magnitude, which hints at differences regarding the detection process and not at issues of the implemented method itself.

Some considerations should be made about the MFS detector. Ideally, each channel would be like a compartment with a very well defined domain in a specific energy range. This is not the case. MFS detector plates were built too large for the implemented collimator setup, making it so that particles that cross the upper walls near the collimator are also detected. Because these particles have to cross through the walls (or layers of the collimator) they lose energy to the medium, hitting the trackers with less energy than they originally had. This makes MFS register hits as having less energy than they actually should have had. Ideally these hits would not be registered, as they are missing the collimator. This effect can be seen on MFS response functions, where supposedly low energy only channels are very sensitive to high energy particles. The data used to obtain the fluxes would be more reliably unfolded if the response functions had more of a step-function like shape.

For future work, it would be interesting to try and take into account electron noise on proton channels and vice-versa. These contaminations can be clearly seen on proton data (and they propagate to the obtained fluxes) as the day/night oscillations of electrons are visible there.

Regarding electron detection, channels 6 and 7 were practically useless because they didn't register statistically relevant data. Channels 4 and 5 were also quite weak statistically-wise. This is supported by their respective response functions - they show much lower detection efficiency to electrons up to 5 MeV, when compared with the first three channels. This meant that the fluxes were mostly obtained from data from channels 1, 2 and 3 during the SEP event and from only channel 1 on the uneventful baseline period. This is clearly not an ideal scenario. Response functions were based mostly on simulations, so in order to improve results more beam test data would be needed to have a better understanding of the detector's behaviour, particularly near the channels thresholds. If another detector has to be sent to GEO, it would be advantageous to try to implement it so as to have more lower energy electron channels (while discarding higher energy channels, if needed). This would distribute the data from channels 1, 2 and 3 to more different channels. If the detector plates/collimator issue were to also not be present, proton channels would also be likely to have better defined domain windows, allowing for an easier data analysis.

Bibliography

- [1] European Space Agency. *Alphasat - Overview*. [online] Available at: http://www.esa.int/Our_Activities/Telecommunications_Integrated_Applications/Alphasat/Overview [Accessed 14 Jun. 2016].
- [2] European Space Agency. *Alphasat - Environmental Testing and Radiation Sensor*. [online] Available at: http://www.esa.int/Our_Activities/Telecommunications_Integrated_Applications/Alphasat/Environmental_Testing_Radiation_Sensor [Accessed 14 Jun. 2016].
- [3] Laboratório de Instrumentação e Física Experimental de Partículas. *AlphaSat TDP-8 MFS Data Analysis, Consolidation and analysis of radiation ground test data and Monte Carlo Simulation*, 2015.
- [4] European Space Agency. *Alphasat TDP#8: Environment and Effects Facility (AEEF) — ESA's ARTES programme*. [online] Available at: <https://artes.esa.int/projects/alphasat-tdp8-environment-and-effects-facility-aeef> [Accessed 14 Jun. 2016].
- [5] European Space Research and Technology Centre. *Flight Data Analysis of TDP8 radiation experiments on-board ALPHASAT*, 2015. Statement of Work.
- [6] Pinto. M. *Development of a Directionality Detector and Radiation Hardness Assurance for RADEM, the ESA JUICE mission radiation Monitor*. PhD thesis, IST, July 2019.
- [7] Arruda, L., Gonçalves, P., Carvalho, F., et al. "Electrons in GEO measured with the ESA Multi-Functional Spectrometer during the January 2014 SEP". *IEEE Transactions on Nuclear Science*, 65:1540 – 1545, Aug. 2018.
- [8] efacec, Engenharia e Sistemas, SA, 2019.
- [9] European Space Research and Technology Centre. *<AlphaSat TDP-8 MFS Particle Spectrometer Data Analysis >, Appendix 1 to ESA RFQ 3-14025/13/NL/AK*, 2013. Statement of Work.
- [10] efacec, Engenharia e Sistemas, SA. *Volume I, Technical Proposal.*, 2013. AlphaSat TDP-8 MFS Data Analysis Proposal.
- [11] *In-Flight Data Analysis*. [online] Available at: <http://ifdatdp8.efacec.com/>.

- [12] L. Arruda and P. Gonçalves. "SEP Protons and Electrons in GEO with the ESA MultiFunctional Spectrometer". *Proceedings of Science*, 2015.
- [13] Paul Scherrer Institute. *The Standard Radiation Environment Monitor*. [online] Available at: http://srem.web.psi.ch/html/srem_home.shtml.
- [14] Bourdarie, S., and Xapsos, M. "The Near-Earth Space Radiation Environment". *IEEE Transactions on Nuclear Science*, 2008.
- [15] National Oceanic and Atmospheric Administration. *Earth's magnetosphere*. [online] Available at: <https://www.swpc.noaa.gov/phenomena/earths-magnetosphere>.
- [16] National Oceanic and Atmospheric Administration. *Coronal Mass Ejections*. [online] Available at: <https://www.swpc.noaa.gov/phenomena/coronal-mass-ejections>.
- [17] Rene Brun and Fons Rademakers, ROOT - An Object Oriented Data Analysis Framework, Proceedings AIHENP'96 Workshop, Lausanne, Sep. 1996, Nucl. Inst. & Meth. in Phys. Res. A 389 (1997) 81-86. See also <http://root.cern.ch/>.
- [18] J. D. Sullivan. Geometrical Factor and Directional Response of Single and Multi-Element Particle Telescopes. *Nuclear Instruments and Methods*, (95):5–11, February 2015.
- [19] Mewaldt, R. A., et al. Proton, helium, and electron spectra during the large solar particle events of October-November 2003. *Journal of Geophysical Research*, 110, 2005.
- [20] James. F. *MINUIT – Function Minimization and Error Analysis*. CERN, March 1994. Reference Manual.
- [21] Cowan. G. *Statistical Data Analysis*, chapter 6 - "The method of maximum likelihood". Clarendon Press, 1998.
- [22] NOAA Space Environment Services Center. *Solar Proton Events Affecting the Earth Environment*. [online] Available at: <https://umbra.nascom.nasa.gov/SEP/>.
- [23] National Aeronautics and Space Administration. *Solar Storm and Space Weather - Frequently Asked Questions*. [online] Available at: <https://www.nasa.gov/> [Accessed 11 March. 2019].
- [24] National Aeronautics and Space Administration (NASA). *GOES N Series Data Book*, November 2009.